

Systematically Measuring Ultra-diffuse Galaxies (SMUDGes). I. Survey Description and First Results in the Coma Galaxy Cluster and Environs

Dennis Zaritsky ¹ , Richard Donnerstein ¹, Arjun Dey ² , Jennifer Kadowaki ¹ , Huanian Zhang (张华年) ¹ , Ananthan Karunakaran ³ , David Martínez-Delgado ^{4,5} , Mubdi Rahman ⁶ , and Kristine Spekkens ^{3,7}

Steward Observatory and Deput ment of Astronomy, University of Arizona, 933 N. Cherry Ave., Tucson, AZ 85721, USA; dennis zuritsky ©gmail.com

NOAQ, National Optical Astronomy Observatory, 950 N. Cherry Ave., Tucson, AZ 85719, USA; dennis zuritsky ©gmail.com

NOAQ, National Optical Astronomy Observatory, 950 N. Cherry Ave., Tucson, AZ 85719, USA; Deputtment of Physics, Engineering Physics and Astronomy Queen's University Kingston, ON K7L 3N6, Canada

Astronomisches Rechen-Institut, Zentrum für Astronomie, Königstuhl 17, D-69117 Heidelberg, Germany

Max. Planck-Institut für Astronomie, Königstuhl 17, D-69117 Heidelberg, Germany

Deputtment of Physics and Space Science Royal Military College of Canada P.O. Box 17000, Station Forces Kingston, ON K7K 7B4, Canada

Received 2018 September 12; revised 2018 October 22; accepted 2018 November 6; published 2018 December 26

Abstract

We present a homogeneous catalog of 275 large (effective radius \gtrsim 5,73) ultra-diffuse galaxy (UDG) candidates lying within an \approx 290 square degree region surrounding the Coma Cluster. The catalog results from our automated postprocessing of data from the Legacy Surveys, a three-band imaging survey covering 14,000 square degrees of the extragalactic sky. We describe a pipeline that identifies UDGs and provides their basic parameters. The survey is as complete in these large UDGs as previously published UDG surveys of the central region of the Coma Cluster. We conclude that the majority of our detections are at roughly the distance of the Coma Cluster, implying effective radii \geqslant 2.5 kpc, and that our sample contains a significant number of analogs of DF44, where the effective radius exceeds 4 kpc, both within the cluster and in the surrounding field. The g-z color of our UDGs spans a large range, suggesting that even large UDGs may reflect a range of formation histories. A majority of the UDGs are consistent with being lower stellar mass analogs of red sequence galaxies, but we find both red and blue UDG candidates in the vicinity of the Coma Cluster and a relative overabundance of blue UDG candidates in the lower-density environments and the field. Our eventual processing of the full Legacy Surveys data will produce the largest, most homogeneous sample of large UDGs.

Key words: galaxies: evolution – galaxies: fundamental parameters – galaxies: structure Supporting material: machine-readable table

1. Introduction

To test the dark matter paradigm and provide boundary conditions for theories of galaxy formation, the astronomical community has been striving to measure the mass-to-light ratio (M/L) of galaxies for over 40 yr (e.g., Roberts 1976; Rubin et al. 1978). As of a couple of years ago, the developed consensus was that M/L within the luminous portion of galaxies increases dramatically only when one considers extremely low mass galaxies, such as the dwarf spheroidal and ultra-faint satellites of the Milky Way, for which M/L reaches values of several hundreds or even above a thousand in solar units (Wolf et al. 2010). That consensus has recently been challenged by the discovery of apparently massive, low surface brightness, dark-matter-dominated galaxies (van Dokkum et al. 2015a), broadly referred to as ultra-diffuse galaxies (UDGs).

Large galaxies of low surface brightness that elude standard galaxy catalogs have been a focus of study for decades (Disney 1976; Sandage & Binggeli 1984; Impey et al. 1988; Schombert & Bothun 1988; Schwartzenberg et al. 1995; Dalcanton et al. 1997; Sprayberry et al. 1997). Such work had even occasionally highlighted physically large low surface brightness galaxies such as Malin 1 (Impey & Bothun 1989). Recently, ever more sensitive observations (see Koda et al. 2015; Mihos et al. 2015; Muñoz et al. 2015; Lee et al. 2017; Román & Trujillo 2017a; Shi et al. 2017; van der Burg et al. 2017; Venhola et al. 2017; Wittmann et al. 2017; Greco et al. 2018) have helped investigators reach even fainter surface brightnesses and, in the case of the Coma Cluster survey by van

Dokkum et al. (2015a), identify many such galaxies that are large and quiescent. Because the galaxies in that particular study are clustered on the sky about the Coma Cluster, distance by association allowed those investigators to convert angular sizes to physical ones. This aspect is critical because redshift measurements become increasingly difficult as we focus our attention on galaxies with ever lower surface brightnesses. Spectroscopic redshifts exist for only a handful of these galaxies and, for the most part, confirm the estimated distances (van Dokkum et al. 2015b; Kadowaki et al. 2017; Alabi et al. 2018). With physical sizes in hand, van Dokkum et al. (2015a) found that their UDGs are surprisingly large, including many systems with effective radii, r, as large as that of the Milky Way. The survival of such systems in the cluster tidal field suggests that these objects are dark matter dominated. Analogous systems, of somewhat brighter surface brightness and smaller size, had previously been found in the Perseus Cluster (Penny et al. 2009), and the tidal argument was used there as well to infer large dark matter content.

To demonstrate that the large size of some of the UDGs connotes correspondingly large mass requires independent mass estimates. In the case of one Coma UDG, DF44, a stellar velocity dispersion was subsequently measured (van Dokkum et al. 2016). The velocity dispersion is indeed consistent with that expected if that galaxy lies in a massive dark matter halo, but the measurement is taken at small radius relative to the calculated virial radius and so weakly constrains the total halo mass. Furthermore, the exposure time required to obtain this

measurement was extreme, and analogous measurements now exist for only a couple of other UDGs (Beasley et al. 2016; van Dokkum et al. 2017). Exploiting the relationship between the number of globular clusters and total galaxy mass established for normal galaxies (Blakeske et al. 1997; Georgiev et al. 2010; Harris et al. 2013, 2017; Forbes et al. 2016; Zaritsky et al. 2016) provides an alternate avenue for estimating the total masses of larger samples (see Amorisco & Loeb 2016). The large populations of globular clusters found in some UDGs support the conjecture that those UDGs lie in massive $(M > 10^{11} M_{\odot})$ dark matter halos (van Dokkum et al. 2017). Lastly, the application of galaxy scaling relations also supports the conjecture that the largest UDGs are indeed massive (Zaritsky 2017).

As these intriguing results developed, other studies have concluded that UDGs are predominantly low-mass galaxies (Amorisco et al. 2018; Sifón et al. 2018). As in any astronomical population, the small, low-mass objects dominate by number over the large, massive ones. This phenomenon is clear in the comparison of the sizes and luminosities of the van Dokkum et al. (2015a) and Yagi et al. (2016) Coma Cluster UDG samples. However, the details of the UDG mass distribution are critical in discriminating between the variety of formation models that have already been developed, which invoke a range of physical phenomena such as environmental quenching, feedback, and high specific angular momenta, to explain both the low apparent star formation efficiencies and large sizes of UDGs (Yozin & Bekki 2015; Agertz & Kravtsov 2016; Amorisco & Loeb 2016; Di Cintio et al. 2017; Carleton et al. 2018; Chan et al. 2018). Arguments about the nature of UDGs and their formation history should bear in mind that UDGs, being selected solely by surface brightness, are likely to include diverse objects and do not have a single origin story (Zaritsky 2017; Ferré-Mateu et al. 2018; Lim et al. 2018).

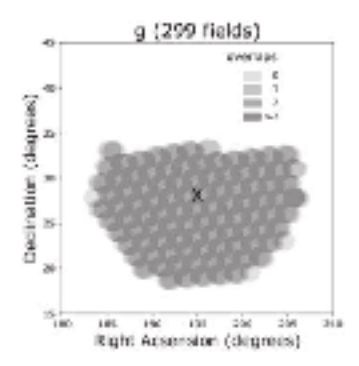
This large range of properties among UDGs and the extensive literature history of low surface brightness galaxies already cited raise the question whether the term UDG is simply a renaming of an already-identified class of galaxy, such as the Low Mass Cluster Galaxy (LMCG) class presented by Conselice et al. (2003). It is early in the detailed internal study of these objects, but the physically largest of these, with halo masses that are inferred to be close to that of an L* galaxy and globular cluster populations to match, appear to be a new category of object, or at least represent a new emphasis. Unfortunately, the current UDG definition, based on central surface brightness, $\mu_{s,0} \geqslant 24 \text{ mag arcsec}^2$, and effective radius, $r_e \geqslant 1.5$ kpc, probably returns a set of objects that have significant overlap with cluster dE and dSph galaxies that have been studied previously (e.g., Sandage & Binggeli 1984; Conselice et al. 2003; Penny et al. 2009). With time, providing that the preliminary results on the few large UDGs already studied extend to a significantly sized population of similar objects, the UDG criteria may be refined to reflect a somewhat more distinct population that may not be either of low mass or exclusively in clusters. For a graphical overview comparing different galaxy populations, we refer the reader to Figure 12 of Greco et al. (2018).

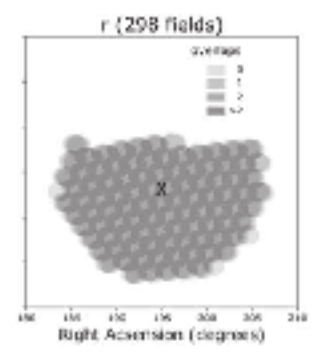
We seek to identify as extensive a sample of physically large UDGs as possible across all environments to establish the characteristics of this population. The largest UDGs are extremely interesting for dark matter studies because (1) they may be dark matter dominated at all radii; (2) when compared to ultra-faint $(M_V > -8 \text{ mag})$ galaxies, which are also dark matter dominated throughout, their expected large internal velocities (>30 km s⁻¹) can ultimately be measured to better relative precision; (3) unlike for the ultra-faint galaxies, there is a parallel sequence of galaxies (normal high surface brightness galaxies of the same total mass) that can be used to help us unravel the effects of baryonic physics on the dark matter distribution; (4) in contrast to dwarf galaxies, their large total mass makes their halos less susceptible to external tides and internal hydrodynamics; (5) they may have satellite systems of their own that can be used to study the dynamics at larger radii than can be probed with integrated light spectroscopy (globular clusters have already been used in this manner, for example, by Beasley et al. 2016); and (6) they are found in all environments (see Makarov et al. 2015; Martínez-Delgado et al. 2016; Leisman et al. 2017; Román & Trujillo 2017a, 2017b; Shi et al. 2017; van der Burg et al. 2017; Wittmann et al. 2017; Greco et al. 2018; Prole et al. 2018), enabling a comparison of dark matter halos across environment.

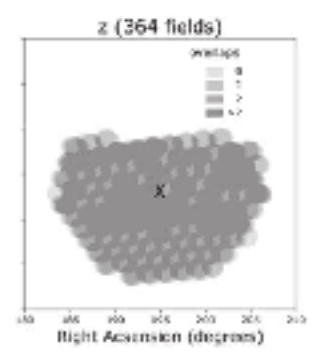
We have begun a survey that will increase the areal coverage and the expected number of large UDGs by orders of magnitude over what is available in the literature today. This work is possible due to the Legacy Surveys imaging data (Dey et al. 2018), which are being obtained in support of the Dark Energy Spectroscopic Instrument project (Schlegel et al. 2011; DESI Collaboration et al. 2016a, 2016b; http://desi.lbl.gov). In this paper, we describe how we are automating the data analysis by presenting results from a relatively small portion of sky, a ~10⁶ projected radius region around the Coma Cluster, to describe our survey and demonstrate what might be expected of the full survey. We are aiming to ultimately make the intermediate steps public, in addition to the final catalog. We find that our processing generates UDG catalogs that are already competitive with the best published surveys in terms of identifying these large UDGs out to the distance of the Coma-Cluster. In Section 2 we describe the publicly available data. In Section 3 we describe our procedure for removing the visible, high surface brightness objects from the images, for smoothing the residuals to increase the signal-to-noise ratio (S/N) of diffuse sources, for identifying real sources, for distinguishing between UDGs and other astronomical sources that manifest as low surface brightness enhancements, and for obtaining parameter estimates. In Section 4 we describe the findings, focusing on the distribution of UDGs both on the sky and along the line of sight within this volume, and the size and color distribution. We adopt a standard ACDM cosmology when necessary with $H_0 = 70 \text{ km s}^{-1} \text{ Mpc}^{-1}$, $\Omega_m = 0.3$, $\Omega_{\Lambda} = 0.7$. To be consistent with van Dokkum et al. (2015a), we assume an angular distance of 98 Mpc to the Coma Cluster, which implies a physical to angular scale of 0."475 kpc-1. The corresponding luminosity distance is 102.7 Mpc. All magnitudes are on the AB system (Oke 1964; Oke & Gunn 1983).

2. The Data

In preparation for the DESI program, the DESI collaboration has undertaken the Legacy Surveys, a deep three-band $(g=24.7, r=23.9, \text{ and } z=23.0 \text{ AB mag}, 5\sigma \text{ point-source limits})$ imaging survey using DECam at the CTIO 4 m (DECaLS), an upgraded MOSAIC camera at the KPNO 4 m (MzLS, Mayall z-band Legacy Survey), and the 90Prime camera at the Steward Observatory 2.3 m telescope (BASS, Beijing-Arizona Sky Survey). This survey will be roughly







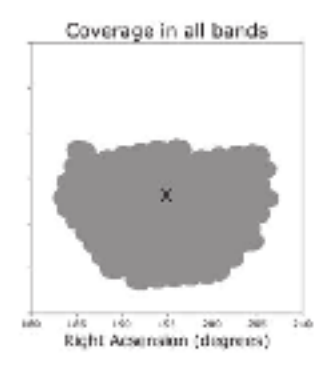


Figure 1. Available data, as of 2018 April 1, in the g, r, and z bands within 10° of the Coma Cluster. In the first three punels, the gray scale denotes the number of the combined set of exposures. The rightmost punel shows regions for which we have coverage in all three filters. The dark, central cross marks the center of the Coma Cluster.

2 mag deeper than the Sloan Digital Sky Survey (SDSS) and is fully described by Dey et al. (2018). The original planned footprint has 9000 deg² observed by DECaLS and 5000 deg² observed by MzLS and BASS. DECaLS, MzLS, and BASS data are already publicly available at the National Optical Astronomy Observatory (NOAO) science archives⁸ and the Legacy Surveys website (legacysurvey.org). Here we present the 275 large (effective radii $r_e \gtrsim 5.93$, corresponding to physical values $\geqslant 2.5$ kpc at the distance of Coma) UDG candidates identified within an $\approx 10^\circ$ radius of the Coma Cluster using publicly released, reduced data from the DECaLS survey that were available as of 2018 April 1. In the future, our work will also include analysis of public BASS and MzLS data, but in this introductory study we focus exclusively on DECaLS data.

DECam consists of 62 imaging CCDs arranged in a hexagonal pattern covering 3 deg² with a pixel scale of 0,°263 (Flaugher et al. 2015). During the period covered by this study, 60 or 61 of the 62 CCDs were available for analysis. Exposure times range from 40 to 250 s, varying with observation conditions to reach the specific 5σ point-source criteria in two out of three exposures. We use the images made available online via NOAO, which have previously undergone calibration and processing (InstCal) via the DECam Community Pipeline (Valdes et al. 2014). We utilize both the object and data quality masks for foreground subtraction and UDG detection as described further below. Parameter values used in calculations such as exposure times, zero points, and pixel scales are obtained from the FITS headers.

The Coma Cluster lies near the northern boundary of the DECaLS survey footprint at a decl. of about $+30^{\circ}$, and, as such, the 10° region around Coma that we target for study is cropped (Figure 1). Nevertheless, the available data even within this truncated region, which is not yet the complete set intended for DECaLS, already consist of 974 separate DECam fields in three different filters (g, r, and z), of which 13 were flagged as bad exposures by the DESI collaboration. The remaining 961 fields (58,320 separate CCD exposures) provide coverage for about 290 deg 2 in all three bands. We began with an analysis of the Coma Cluster to enable direct comparison with previous UDG searches.

3. Uncovering Diffuse Sources

Various factors, some natural and some instrumental, limit our ability to locate low surface brightness galaxies. Previous studies have applied innovations to focus on different limiting aspects; examples include drift scanning to address issues of image uniformity (Gonzalez et al. 2001), specialized telescope baffling and new algorithmic approaches to address issues of scattered light (Mihos et al. 2015), and refractive telescopes with new lens manufacturing techniques to mitigate the wings of the point-spread function (PSF; Abraham & van Dokkum 2014). Here we face the principal challenge, given the use of archival data, that neither the instrumentation nor observations were optimized for the detection of low surface brightness galaxies.

Despite this challenge, these data provide several key advantages over previous and ongoing surveys. First, such a large survey allows us to be relatively conservative in masking and still retain the ability to identify a large number of sources. Second, the multiple pass observational strategy provides some averaging over sky fluctuations. Third, the availability of images taken through three different filters, a luxury in low surface brightness surveys, enables us to confirm sources in different passbands and potentially to use color as a discriminant against contamination. Fourth, the relatively high spatial resolution (≤1"), which is typically not considered to be necessary when searching for large, diffuse sources (van Dokkum et al. 2015a), enables us to more effectively clean contaminating sources, particularly highly correlated, distant galaxies, which commonly produce low surface brightness enhancements in such searches (Gonzalez et al. 2001). Finally, the Legacy Surveys cover most of the extragalactic sky, enabling the most comprehensive survey for UDGs from both hemispheres.

In this section, we outline our data analysis process and demonstrate that we are effectively complete in our detection of the galaxies found in the core of the Coma Cluster using the Dragonfly telescope (van Dokkum et al. 2015a) and, to a large degree, those found using the significantly more sensitive Subaru HyperSuprime images (Koda et al. 2015; Yagi et al. 2016). The majority of the galaxies that we miss from the Koda et al. (2015) and Yagi et al. (2016) studies are those that do not appear to match our selection criteria, not ones that we fail to detect. Therefore, our analysis of the DECaLS data will yield UDG candidates of the sizes and surface brightnesses highlighted in the van Dokkum et al. (2015a) study over thousands of square degrees of sky.

archi ve nouo edu

The dominant source of effective noise complicating the detection of low surface brightness objects in these images are resolved stars and galaxies. These can be exacerbated by resulting artifacts such as diffraction spikes and bleeds. In some cases the nature of the source itself, such as the tidal tails and shells that surround some galaxies, complicates the identification of low surface brightness sources. Although aggressive masking reduces contamination from these foreground and background sources, such masking can also make it difficult to recover low surface brightness galaxies extending over relatively large angular scales. Therefore, we take care to preserve low surface brightness, large-scale structures while reducing the effects of high surface brightness objects. Our approach requires several steps to replace the extended wings of bright foreground and background objects with a model, rather than straightforward masking of large areas.

3.1. Image Preprocessing

We carried out the image processing and analyses on the Ocelote cluster at the University of Arizona High Performance Computing center." Before removing all detectable foreground/background sources, it is necessary to reduce the dominant contaminating artifacts. These include image defects, halos and ghosts of extremely bright stars, and amplifier differences. Image defects (cosmic rays, bad pixels, bleed trails, etc.) already identified in the data quality mask provided by DECam Community Pipeline are replaced with neighboring pixels that have been smoothed using a Gaussian filter, excluding the region of the defect. Noise is then added to these pixels using the statistical properties of the image background. Because each DECam CCD reads out using two channels (Flaugher et al. 2015), there are differences in gain and bias level between the two sides of the CCD. Although residual differences after pipeline processing are usually minor, even a small difference can make it difficult to characterize low surface brightness objects near the CCD center and becomes obvious when smoothing the data on large scales. We compensate for this asymmetry by attributing any measured difference to an error in the adopted bias level and add a correction to one side of the image. We estimate the value of the correction by aggressively masking all objects on the image and computing the difference in the means in two 100-pixelwide strips along the CCD midline. Extended wings of very bright stars can extend even beyond the masked regions; therefore, this process is performed both before and after subtracting these wings, and it is described further below.

We use the data quality mask and the process described next for detecting saturated stars and those with diffraction spikes. First, we generate a problem star candidate list using SExtractor (hereafter SE; Bertin & Amouts 1996) with per-pixel detection threshold and minimum area settings of 2σ and 500 pixels, respectively. We retain detections with a minor-to-major axis ratio >0.8. If the data quality mask flags saturated pixels within a candidate detection footprint, we classify it as a saturated star. A different approach is needed to identify stars without saturated pixels. The four diffraction spikes generated by the telescope lie at about 45° from the vertical and horizontal CCD axes. For each star candidate, we divide a region extending from 0.5 to 1.2 Kron radii into 16 22°.5 wedges starting at 11°.25 from the long axis of the CCD. Diffraction spikes will create a large variance among the mean fluxes within these wedges. If at least three out of four wedges containing potential diffraction spikes contain more flux than their two abutting neighbors, we classify the object as a problem star.

Correcting for these problem stars is complicated because the profile of very bright objects is noticeably asymmetric and can be a function of the readout direction. Our process involves two steps. First, we measure the object centroid, axis ratio, and peak amplitude by fitting a Gaussian to its radial brightness profile between one and two Kron radii independently along the horizontal and vertical axes. We exclude pixels that are flagged in the data quality mask. Because we are only interested in defining centers and eccentricities at this stage, the model choice is not critical. Second, we use these results to fit the extended wings between 5 and 30 FWHM with an elliptical Moffat profile, which is then subtracted from the image. We present an example result in Figure 2.

3.2. Object Identification, Masking, and Removal

Next, we subtract resolved foreground/background objects to remove sources of "noise" identified in a smoothed image of the sky. While it is possible to aggressively mask these sources (Gonzalez et al. 2001), such aggressive masking with the deep DECaLS images would eliminate too much sky and complicate UDG detection. At the other extreme, one could aim to model and subtract all detected sources. Unfortunately, it is impossible to model many bright sources well enough to produce accurate residuals at the flux levels of UDGs because galaxies tend to be irregular at such surface brightnesses. While we will never be able to identify a low surface brightness source coincident with a bright star or galaxy (Figure 2), our goal is to subtract the wings of foreground/background sources sufficiently well that we can be more limited in our masking.

The objects that we do subtract are identified using SE with a per-pixel detection threshold of 3σ above sky and a minimum area of 6 pixels. These values are a compromise that enables detection of all but the faintest objects that are visible to the eye in the images and yet does not detect UDGs. It is possible that these criteria, as well as others described below, will need modification when we examine fields with different source densities. All detections are initially replaced with a temporary elliptical mask with a size that is a function of its peak flux. As discussed below, this temporary mask is eventually replaced with a model of the object's surrounding background. We chose the mask size such that its edge has a value of 8 ADU above sky when fitted with an elliptical Moffat function. While this value produced good results over a range of S/N and different bands, it is not optimized for these parameters and will likely be adjusted after completeness studies. Its purpose is to limit the size of the mask while still allowing the source wings outside of the masked region to be approximated by an elliptical exponential function, $He^{-\gamma r}$, where H is the peak flux and γ is a scale factor. The radius r is calculated using

$$r = \left[\left(\frac{\cos \theta^2}{a^2} + \frac{\sin \theta^2}{b^2} \right) (x - x_0)^2 + \left(\frac{\sin \theta^2}{a^2} + \frac{\cos \theta^2}{b^2} \right) (y - y_0)^2 + 2 \sin \theta \cos \theta \left(\frac{1}{a^2} - \frac{1}{b^2} \right) (x - x_0) (y - y_0) \right]^{1/2}, \quad (1)$$

https://docs.hpc.urizona.edu/display/UAHPC/Compute+Resources

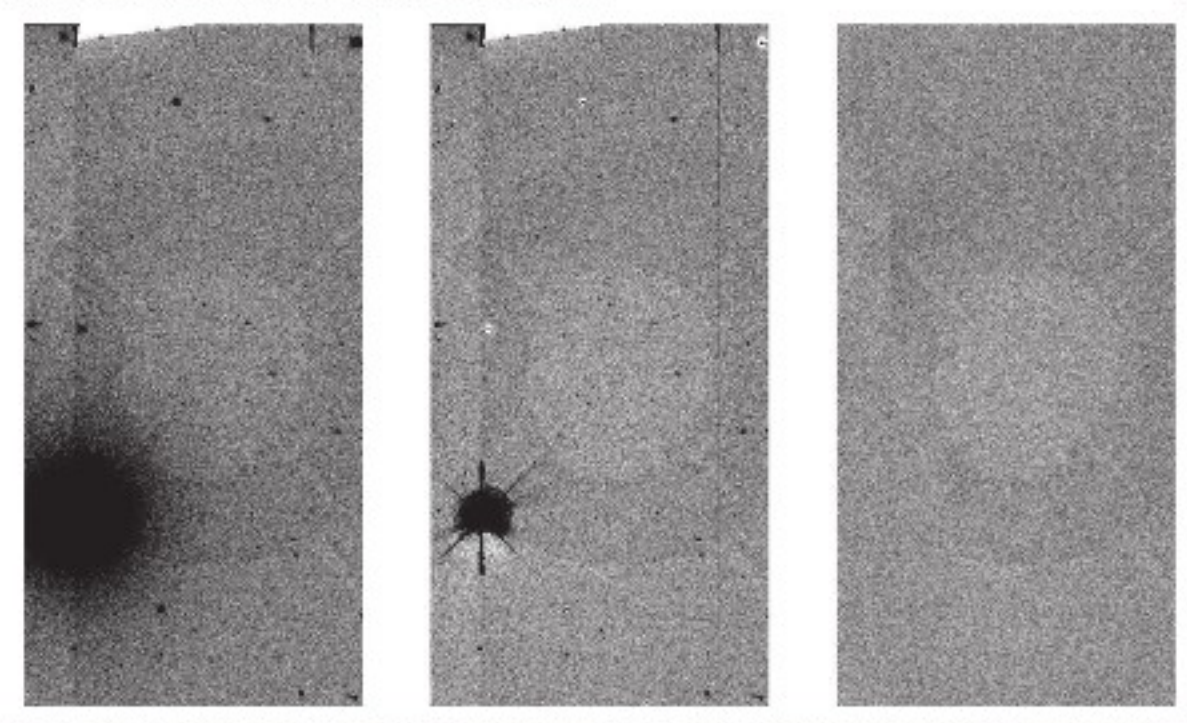


Figure 2. Results after processing an image with an unusually bright object. The images span 18.3 × 9.1 arcmin. Left panel: original CCD image containing a bright star with extended wings and associated pupil ghost. Middle panel: the extended wings of that star have been subtracted even for this bright an object. Right panel: the fully processed image shows the residual pupil ghost, as well as faint evidence of the original star. The ghosts are difficult to model because they are field position dependent. Despite our processing, most of this image is inadequate for detecting faint UDGs, but fortunately such cases appear rare given our extensive visual inspection of candidates. The bright feature in the upper left edge of the prior two panels was identified and replaced during the subtraction procedure.

where a and b are the major and minor axes of the Moffat function, θ is its position angle, and x_0 and y_0 are the center coordinates. The source is assumed to be superimposed on a tilted planar background, S = Ax + By + C, where S is the sky level function, A and B are slopes along the vertical and horizontal axes, and C is the mean sky level. Model fitting is done using the Python software package LMFIT (Newville et al. 2014). We subtract the source model from the surrounding region and replace the masked portion of the source with the tilted background derived from model plus noise estimated from the image. These approximations work very well for most galaxies and stars (Figure 3), although, as shown in Figure 2, they can fail for unusually bright objects. The average total replaced masked area for a CCD is 13.0%, but it did reach levels of over 50% in some regions, such as the center of the cluster. While this process can leave faint residual sources that are not UDGs in the image (Figure 3), the UDGs are unaffected. We refer to these processed images as the "cleaned" images.

3.3. Wavelet Filtering

A key step in detecting UDGs is to spatially filter the cleaned images because UDGs, of the type detected so far, are not particularly faint in terms of total apparent magnitude. While bright objects have been removed from these images, low surface brightness, extended objects must still be detected among the many residual compact sources and background sky noise. A general method for achieving this is to use smoothing to improve the overall S/N for extended sources by decreasing sky noise and then apply 2D filters to enhance signals associated with objects of a particular size. There are various

approaches that can be taken here, including matched filtering if the parameters of the source population are fairly well constrained (e.g., Dalcanton et al. 1997; Gonzalez et al. 2001). Advantages of this approach are that sources with other characteristics are discriminated against and the smoothing is optimized for the intended sources. An alternate approach is "thresholding," where one identifies pixels above a certain threshold level and identifies clusters of such pixels (e.g., Kniazev et al. 2004; Bennet et al. 2017). The advantages of this technique include that no prior knowledge (or bias) of the source population is necessary and that it is computationally efficient and simple to implement and model. We opt for yet a third approach.

Wavelet transforms enable us to isolate objects at different scales with a tailored filter. Their ability to spatially isolate objects by size and location in noisy fields has led to their application in astronomy for detection of faint objects in complex environments (Damiani et al. 1997; Starck & Murtagh 2006; Anisimova et al. 2011). We implement a multilevel, stationary wavelet transform using a version of the à trous algorithm as described by Starck & Murtagh (2006). For our discrete smoothing kernel, K, we use the scaled difference of 2D normalized exponentials

$$K = n \frac{e^{-r/k}}{2\pi k^2} - (n-1) \frac{e^{-r/2k}}{8\pi k^2},$$
 (2)

where n is a scaling factor and k defines the radial scale. The first term can be thought of as the constructive term of the kernel that helps increase the S/N of a source of radial scale r = k, and the second term as the destructive term that diminishes the contribution from light at larger scales. This is reminiscent of the unsharp masking technique. The critical

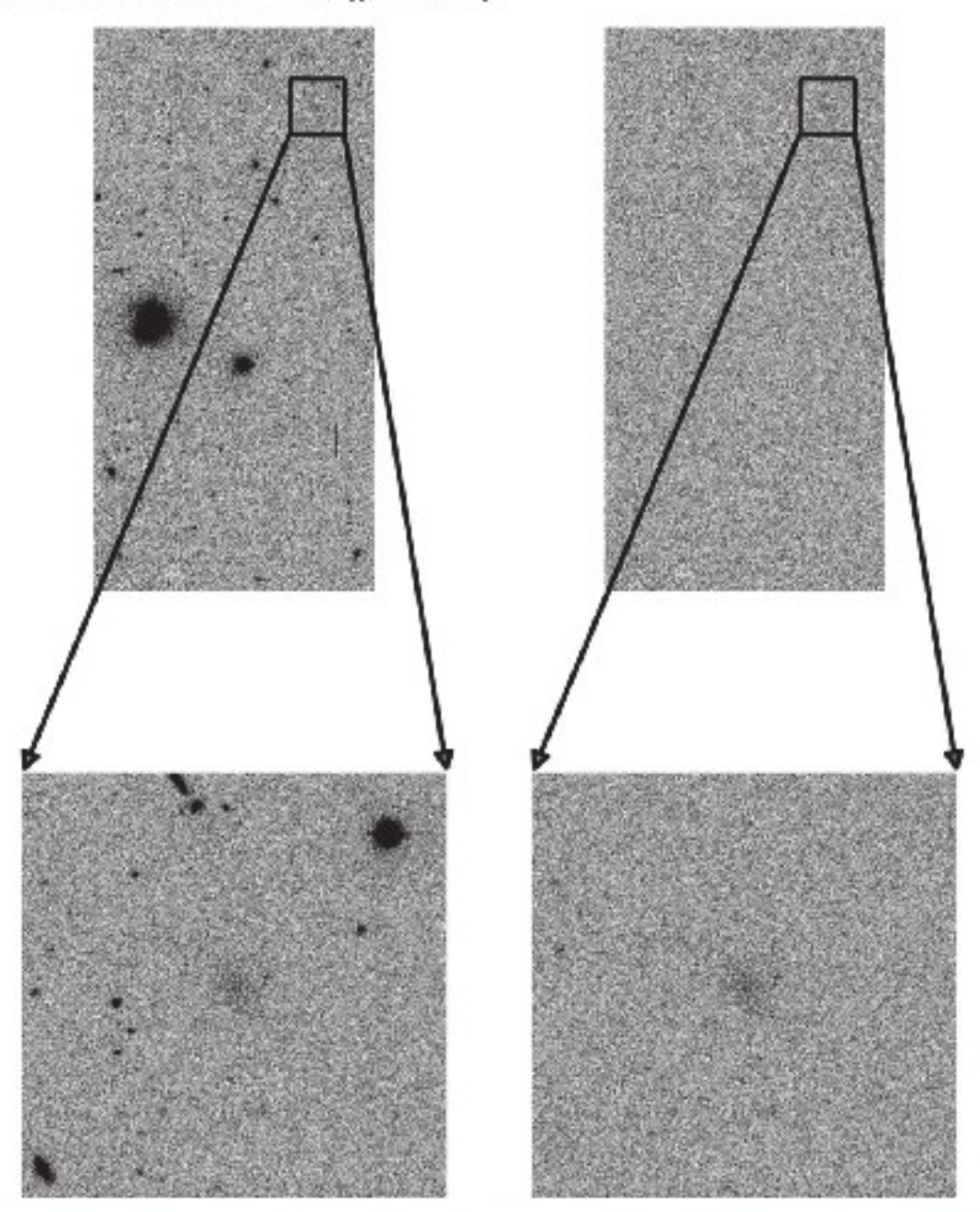


Figure 3. Example of the entire subtraction process applied to one CCD image. The top punels (18.3 × 9.1 arcmin) show the image before and after high surface brightness objects have been removed. The bottom punels (108 × 108 arcsec) are zeomed-in views of the regions outlined in the top punels. The linear stretch is the same in all punels. The most noticeable residual object in the top right punel is a UDG (DF07; van Dokkum et al. 2015a) that lies at the center of the bottom punels. Although the bright objects are removed from the bottom right punel, several faint residual sources were not identified and subtracted owing to the chosen SE threshold levels.

feature is that, unlike smoothing, this approach separates contributions from features at different scales. The scaling factor, n, determines both the steepness and the zero crossing of the kernel. A value of n=1 results in an exponential profile with no zero cutoff. We choose a value of 1.5, which maintains a broad profile with a discrete zero crossing. We use a radial scale, k, of 4.0 pixels for the starting kernel since it has a size profile (FWHM ≈ 1.94) on the order of the smallest objects detectable by DECaLS. New wavelet levels are created by upsampling the kernel in the previous level by a factor of two. Therefore, the kernel for each level, l, is expanded by a factor of 2^{l-1} (the baseline is designated as level one) from its baseline size. For a given scaling factor and radial scale, higher

wavelet levels have broader profiles and will selectively detect larger objects.

An example of this process applied to the image from Figure 3 is shown in Figure 4. The UDG is first visible at wavelet level two and becomes more prominent at larger scales, allowing it to be easily isolated from smaller objects. We find that level four is appropriate for identifying UDG candidates of the size reported in this paper. As seen in Figure 4, objects can be present at different wavelet levels. Relatively compact objects are more prominent in the images filtered at lower wavelet levels, whereas the more extended objects dominate at higher levels. We take advantage of this filtering by using levels two and four to provide an initial list of potential UDGs presented here.

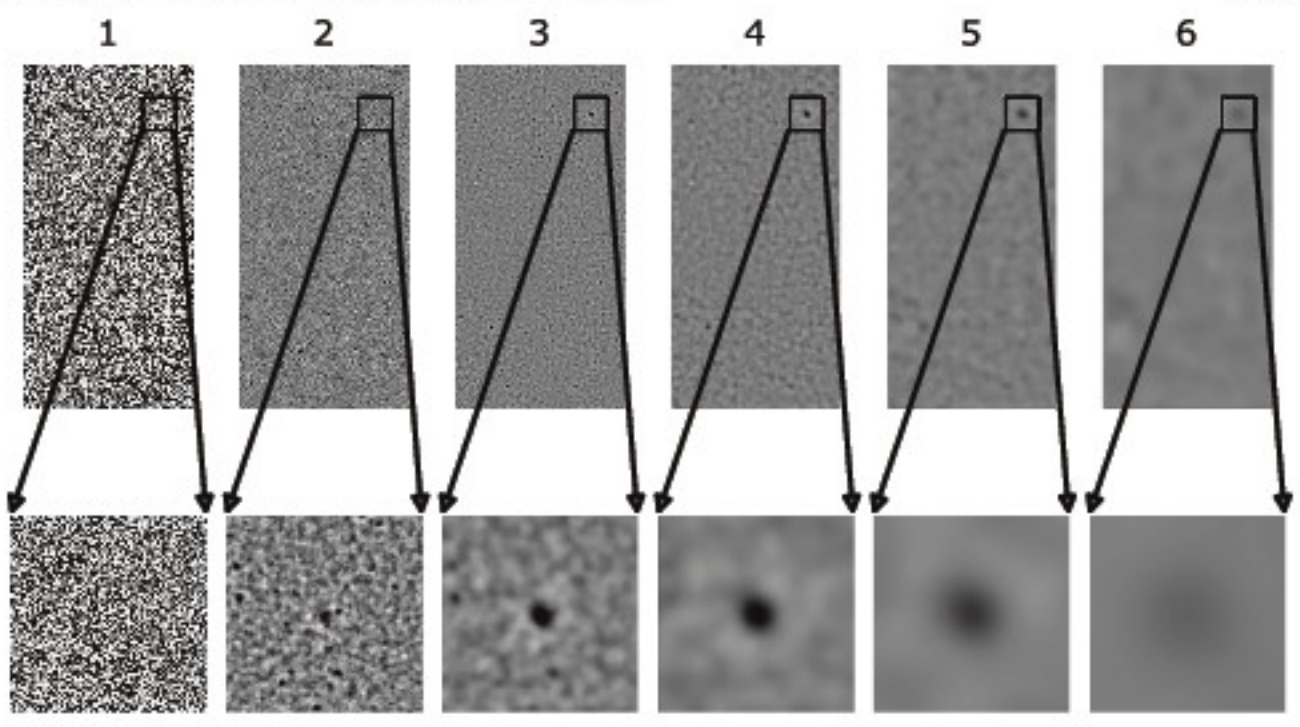


Figure 4. Example of the wavelet process applying a range of levels to the cleaned image from Figure 3. The numbers above each column represent the wavelet scaling level, I. All punels are shown at the same intensity stretch. The contrast is manifestly maximized at certain scales, presumably those that better match the source angular size. Images in the top punels span 18.3 × 9.1 arcmin, and those in the bottom punels span 108 × 108 arcsec.

3.4. Detection, Confirmation, Parametric Fits, and Object Classification

Wavelet filtering and source detection are applied separately to each cleaned image. To detect objects in the wavelet images, we first examine the level four wavelet image. A detection map is created from this image using SEP (Barbary 2016), a set of libraries of stand-alone functions and classes based on SE (Bertin & Arnouts 1996) that can perform many, but not all, of the functions efficiently in memory rather than using slower disk access. This application, rather than SE, is utilized when we are primarily interested in only the detection image and background statistics. We use a threshold of 2.5 times the background noise and a required minimum area of 300 pixels2. These choices reflect a compromise between detecting the faintest objects and minimizing false detections. To filter out small objects with extensions or merged neighbors, we create a separate detection map using the level two wavelet and an SEP threshold of 3 times background noise and a minimum area of 6 pixels. We require that any object present in both detection maps have at least 25% of their peak flux in the level four detection map to be considered a UDG candidate. We further require that the object be no closer than 30 pixels from the image edge, be unrelated to any saturated or bleed pixels flagged in the data quality mask, and have no more than 30% of its area encroached by masks used in the initial object subtraction process. This process results in an initial list of 3,574,596 UDG candidates (see Table 1) for how various processing steps winnow down these candidates.

Candidates need to be confirmed as statistically real, and then the objects need to be classified from among the full range of potential sources that appear as low surface brightness features in the images. We retain UDG candidates only if there are coincident detections among different exposures, regardless of filter, within 2" of the centroid of the group formed by the

Table 1 Scieening Survivors

Process	Candidate Galaxie: 3.574,596		
Wavelet screening			
Object matching	618,028		
Sérsic screening	55,059		
Galfit screening	1079		
Visual screening	275		

coincident detections. Each candidate is tested to see whether it is within 2" of an already-existing grouping of detections or another isolated candidate. If it is related to an existing group, it is merged with that group and any outliers (>2" from the new centroid) are removed. Otherwise, it is merged with the paired detection to form a new group. To minimize duplicates, we compare UDG candidates within 4" of each other and retain only the one with the most individual detections. We will therefore be biased against separating very close pairs of UDGs if they exist. We found 618,028 groups (1,438,367 separate detections) fulfilling these criteria.

As defined by our science aims, our UDG candidates must meet specific size and surface brightness criteria. To obtain rough but reliable estimates of these characteristics, which we will use to do a preliminary candidate screening, we apply the following procedure. We return to the uncleaned images to ensure that our processing did not remove a key component of the candidate UDG that could affect the measurement of its global characteristics. Our first challenge is that in many cases the UDG candidate, particularly if large, is not identified as a single object by SEP (i.e., having a single segmentation map identification number). This problem is markedly reduced by generating a segmentation map using a smoothed version of the uncleaned image. The smoothing kernel we adopt is a Gaussian

with a standard deviation of five pixels. Our second challenge is that there are often contaminating sources nearby. To mask these objects in the fitting, we will use the segmentation map obtained using the smoothed image, with one modification. We remove the object in the center of the segmentation map, presumably the candidate, from the mask. Each detection is separately processed using a 201×201 pixel thumbnail image with the candidate in the center. The segmentation map of the smoothed image is created using SEP with a detection threshold of twice the background noise and a minimum area of 10 pixels. These values represent a compromise between being able to detect the candidate and contaminating objects while avoiding excessive spurious detections. The central candidate is then identified and removed from the mask. Using the leastsq function from the Python SciPy library (Jones et al. 2001), an n = 1 (exponential) Sérsic model is fit to the unmasked pixels in the original uncleaned thumbnail. We choose n = 1 to match the choice of van Dokkum et al. (2015a) for comparison and because that is broadly consistent with empirical determinations for similar objects (Conselice et al. 2003; van der Burg et al. 2016; Yagi et al. 2016). The sky level during fitting is fixed as the mean background determined by SEP.

The resulting parameter estimates from our Sérsic fitting are preliminary. Although they are similar to those produced by GALFIT (Peng et al. 2002) later on, they are generated using only a single image detection rather than co-added images. To avoid rejecting detections that might meet our criteria when more precise estimates are obtained from the co-added images, we now set thresholds that are less strict than those that we will eventually require for our catalog. To be retained as a UDG candidate at this stage, at least two individual detections must result in a fit with an effective radius >4" (~2 kpc at the distance of Coma) and a central surface brightness (μ_0) greater than a value that depends on the band. Because we define a UDG as having a g-band central surface brightness ≥24 mag arcsec⁻², we set the current screening threshold in this band at 23.5 mag arcsec-2. Almost all UDGs will be brighter in the r and z bands, and to avoid excluding potential UDGs in these bands, we set their screening thresholds at 22.5 and 22.0 mag arcsec⁻². A total of 55,059 possible UDGs fulfill all of these criteria.

Next, we do a more detailed and precise examination of the surviving candidates using GALFIT, which is more versatile and provides more information than the basic Sérsic fitting described above. An example of this process is shown in Figure 5. We again return to the uncleaned images, as shown in panel (a), to avoid a situation where part of the candidate was removed by our cleaning procedure. In this case, we simultaneously process all of the images containing the candidate, including those in which nothing was previously detected. We create co-added 201×201 pixel (54 × 54 arcsec) thumbnail images centered on the candidate for the analysis. Co-added images are modeled both separately for each filter and using all images (full stack). Once again we need to mask contaminating objects without rejecting faint structures within the candidate. Our first step in this process is the same as in our Sérsic fitting process described above. We use a Gaussian filter to create a smoothed version of the uncleaned thumbnail and identify the candidate in the segmentation map (panels (b) and (c)). After separately masking negative outliers ($<-2\sigma$), we create a mask using pixels in the segmentation map that are not associated with

the candidate (panel (d)). We refer to this as the preliminary GALFIT mask.

The Gaussian smoothing helps keep the candidate intact during the segmentation process, but it also prevents us from identifying overlying high surface brightness objects. Therefore, in a second step, we create a mask of high surface brightness objects, including those superposed on the candidate (panel (e)). We do this by creating a separate segmentation map of the uncleaned, unsmoothed thumbnail using a detection threshold of 1.5 times the central surface brightness threshold for a band (24.0, 23.6, and 23.0 mag arcsec⁻² for g, r, and z, respectively) with a minimum area of 10 pixels2. This threshold is high enough to avoid detecting portions of a candidate that meet our central surface brightness criteria. We combine this mask and that produced in the first step. This combined mask (panel (f)) may include objects that are physically part of the candidate. Therefore, in a third step, we fit a Sérsic exponential model (panel (g)) to the unmasked regions of the cutout image (presumably containing only the candidate and remaining sky) and subtract the model from a copy of the uncleaned thumbnail to leave only the remaining overlying and peripheral objects (panel (h)). Without additional information it is not possible to unequivocally discriminate between those objects that are part of the candidate and those that are contaminants. However, point sources, with the exception of a nuclear source, are more likely to be independent of the general structure of the candidate, even if physically associated, and so we do not want to consider them during fitting. Masking resolved sources superposed on the candidate could lead to masking of large areas therein, so we opt not to do so.

To implement this discrimination and create a new mask (panel (i)), we use SE with a relative detection threshold of 2.5 and a minimum area of 10 pixels2 to generate segmentation maps (for the different filter co-adds and the full stack) and measure the FWHM of each object in the residual image described above. In the co-added stacks of images in a particular filter, we define the PSF FWHM to be the maximum of the values obtained from the FITS headers of all CCDs contributing to the co-added image. For the PSF FWHM of the full stack, we adopt the average of the PSF FWHM from the individual filter stacks. We assume that any object within the candidate footprint with an SE FWHM > 1.5 times the PSF FWHM is part of the UDG candidate, and it is removed from the mask. This mask does not adequately cover the wings of bright peripheral objects, so we combine this mask with the preliminary GALFIT mask described above (result shown in panel (j)).

The unsmoothed, uncleaned image and the mask (panels (a) and (j)) are supplied to GALFIT. For defining UDGs, we elect to be consistent with the methodology of van Dokkum et al. (2015a) and use a fixed Sérsic index of n = 1 for the model with central surface brightness, μ_0 , calculated from the effective radius, r_e , the ratio of the minor to major axes, b/a, and the apparent total model magnitude. However, as noted below, more general fitting is provided for photometry estimates.

A trimmed list of UDG candidates is generated by selecting those objects that satisfy (1) $\mu_{0,g} \geqslant 24 \,\mathrm{mag\,arcsec^{-2}}$ or alternatively $\mu_{0,z} \geqslant 23 \,\mathrm{mag\,arcsec^{-2}}$ if an observation in the g band is not available; (2) $r_e \geqslant 2.5 \,\mathrm{kpc}$ at the distance of Coma, which corresponds to $\gtrsim 5.73$; and (3) $b/a \geqslant 0.37$. Both

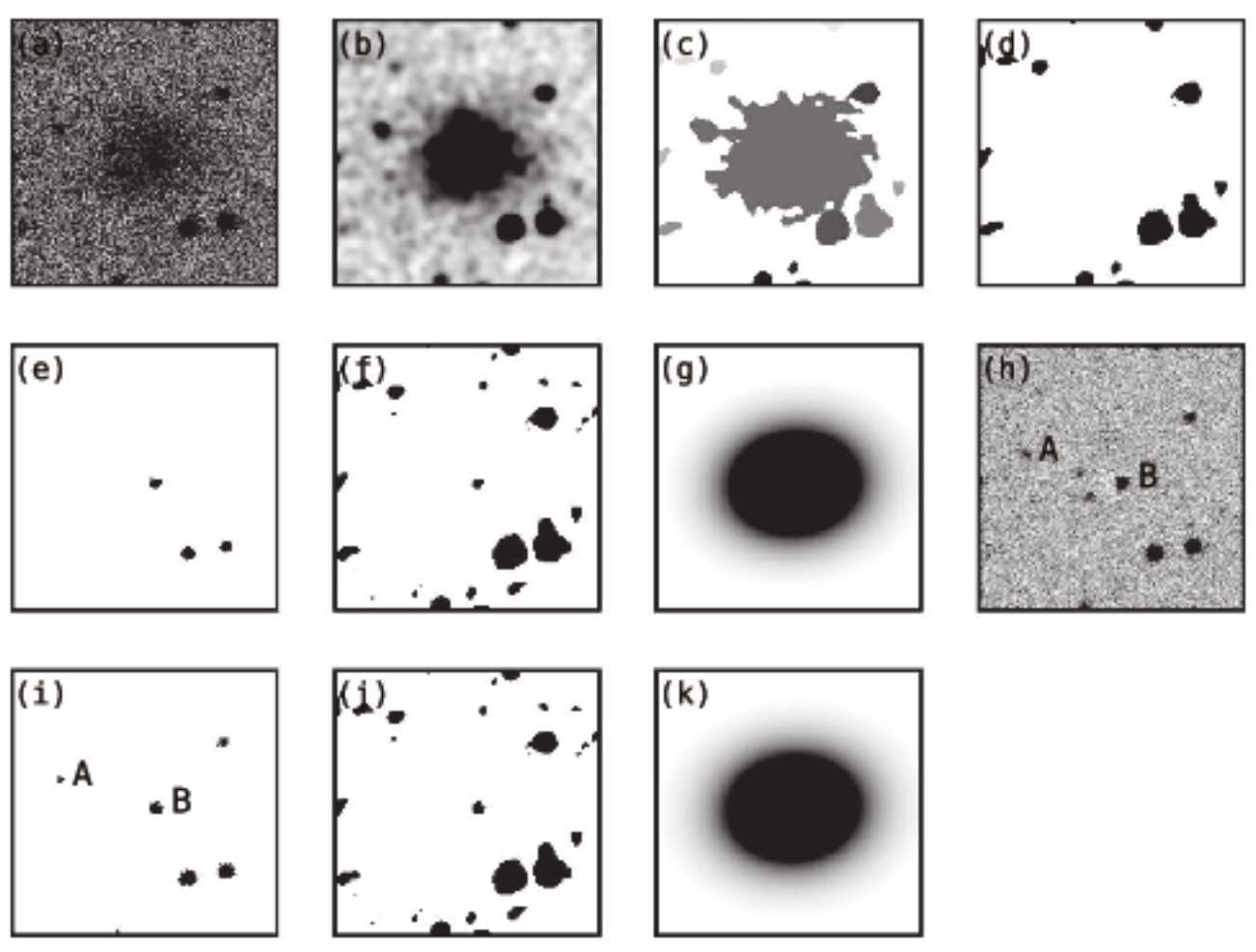


Figure 5. Example of the steps involved in producing the GALFIT model. All punels are 201 × 201 pixels (54 × 54 arcsec). (a) Postage stamp of uncleaned image with the candidate in the center. (b) Gaussian smoothed version of punel (a). (c) Segmentation map of smoothed image. In this punel only, gray scale corresponds to the segmentation numbers. In this case, the candidate is represented by the central, large detection. (d) The detection corresponding to the candidate is removed from the detection map (preliminary GALFIT mask). (e) Segmentation map of uncleaned, unsmoothed image required to detect overlying high surface brightness objects. (f) Mask created by the union of punels (d) and (f), which is used to create a Sérsic model of the uncleaned image. (g) Sérsic model. (h) Residual after subtracting the Sérsic model from the uncleaned image. (i) SE segmentation map of the residual image. (j) Mask created by the union of punels (d) and (i), which is used to create a GALFIT model of the uncleaned image. Both objects A and B shown in punel (h) are within the candidate detection footprint. In punel (i) the SE FWHM of object A is >1.5 times the PSF FWHM, so it is removed from this final mask. For object B, it is <1.5 times the PSF FWHM, so it is kept. See the text for details. (k) Final GALFIT model.

 r_a and b/a are the values obtained from the fully stacked thumbnail. We selected the b/a threshold as a compromise between limiting detections of artifacts (many of which, such as diffraction spikes, are narrow) without sacrificing a significant number of actual UDGs (also see Figure 4(b) in Koda et al. 2015). Only 1079 candidates satisfy these criteria.

Our next step is to sort through the list for possible contaminants. Contaminants may result from artifacts, but they may also be caused by astronomical sources such as extended stellar tails from galaxies, distant galaxy clusters, and nebulae within our own Galaxy. Ultimately, we need this screening to be automatic and reproducible. However, at first we need to develop our understanding of the resulting candidate sample and generate a training sample. To achieve both of these objectives, one of us (RD) visually classified all candidates, removing those that were confidently not UDGs from further review. The 650 rejected objects fall into three main categories: (1) real objects such as peripheral parts of large, bright galaxies (tidal debris, spiral arms), clusters of stars or galaxies, and dust; (2) wings and scattered light from very bright galaxies and stars, and (3) instrument artifacts (pupil ghosts, diffraction

spikes, CCD artifacts, etc.). Examples of rejected detections are shown in Figure 6. Full images and surrounding sky may be seen using the Legacy Survey Sky Viewer. 10

Two of the authors (R.D. and D.Z.) examined the remaining 429 candidates in more detail. They disagreed on the classification of 63 (15%) of these as a UDG; tidal debris; faint, high-redshift galaxy clusters; or fluctuations in background sky (for very faint detections). Arguments for accepting or rejecting objects from this group were independently reviewed by both examiners, and any candidate not acceptable as a UDG to both was rejected. Examples of candidates with initially conflicting classifications are shown in Figure 7, where we also present their final, consensus classification. A total of 285 detections were classified as bona fide UDG candidates. Our initial requirement that candidates be separated by at least 4" to be considered unique objects is inadequate for large UDGs and results in some duplication. Therefore, we perform a final pass that requires that no object be within one r_e of

in legacysurvey.org/viewer

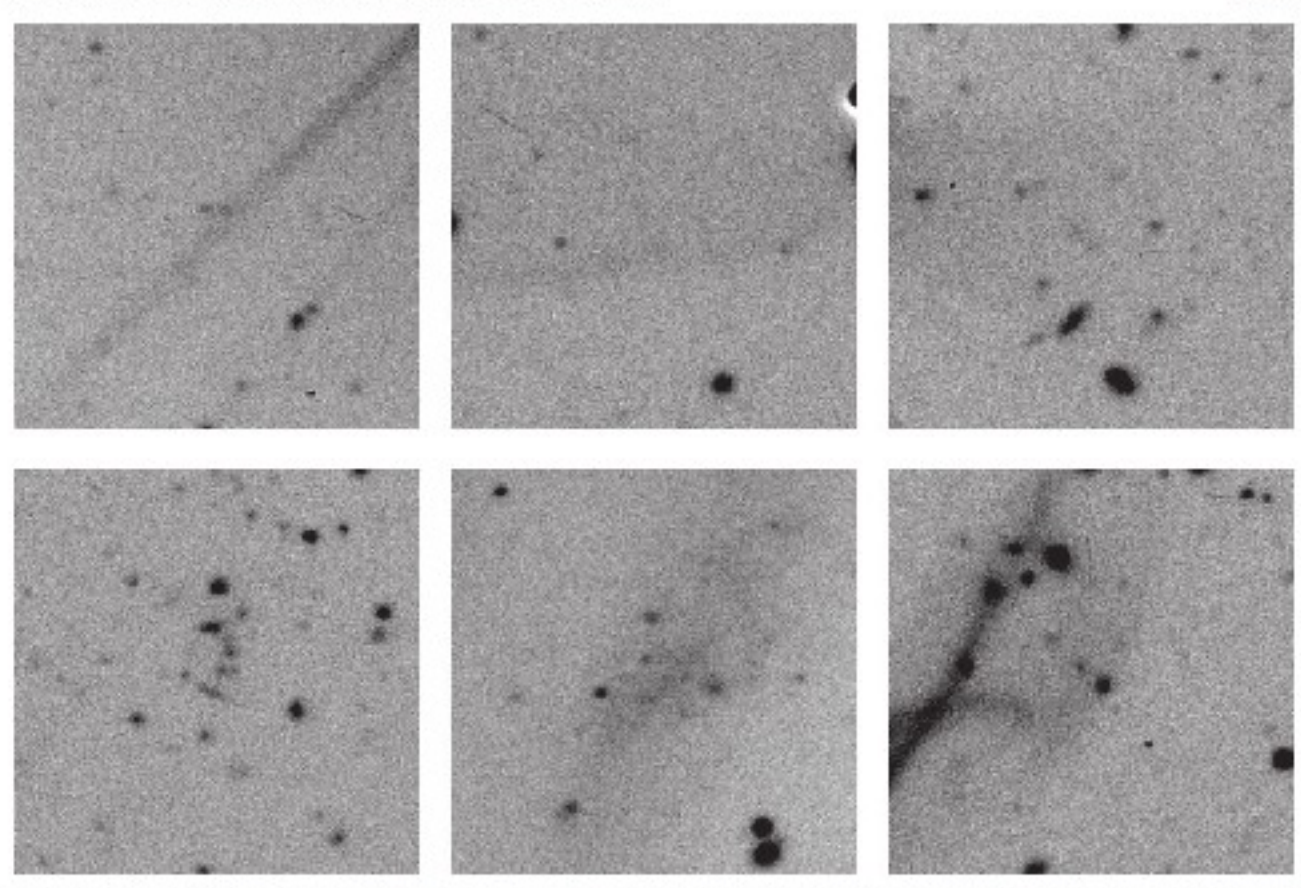


Figure 6. Examples of detections rejected during initial screening. R.A. and decl. of detections are shown in parentheses, following our visual classification. Upper tow from left to right: diffraction spike (184.4079, 28.9644), pupil ghost (185.7454, 25.9153), and scattered light from nearby star (186.0171, 23.965). Lower tow from left to right: cluster of galaxies (185.69, 27.5842), spiral arm of nearby galaxy (192.605, 25.4389), and tidal debris (190.6537, 25.7392).

another candidate. This eliminates eight duplicates, leaving us with a total of 277 potential UDGs.

Because we want to automate classification using a machine learning classifier (see Section 3.5), our visual decisions at this stage were based only on the available thumbnails without viewing surrounding fields, or other survey data, for additional clues. However, as demonstrated in Section 3.5, this restriction can lead to erroneous assignments. Because we do not want obviously incorrect classifications in our catalog, after finalizing the machine learning classifier, we reexamined all 277 potential UDGs in the Legacy Survey Sky Viewer. This review rejected two candidates, giving us 275 UDG candidates in our final catalog.

While our initial GALFIT results are adequate for defining UDGs, more robust modeling is required for the type of photometric analysis presented in Section 4. Therefore, new profiles are created of all 275 confirmed UDGs using GALFIT in a manner identical to above, except that the Sérsic index, n, is allowed to float. The mean value of n is 0.85, the median is 0.73, and the standard deviation is 0.70. In some cases, our further analysis uses magnitudes and colors obtained from these models as specified. There is the danger of strong biases in the photometry of low surface brightness objects. These become particularly apparent at brightnesses significantly below sky level and can result in an overestimate of magnitudes while effective radii and Sérsic indices are underestimated (Häussler et al. 2007). We will revisit the issue of optimizing the choice of photometric approach in upcoming work describing our recovery of simulated sources. For now,

we only discuss broad, qualitative first impressions from these data in Section 4.

3.5. Automated Classification

Confirmation of UDG candidates has typically been done, both in this study and in previous UDG studies (see Koda et al. 2015; van Dokkum et al. 2015a; Greco et al. 2018) on the basis of simple measurements or visual inspection. As documented in the previous section, this can be very time-consuming and subjective. While visual classification is feasible with the limited area surrounding Coma discussed in this paper, it would be impractical for very large regions such as that included in the complete DES1 footprint. Moreover, because of the huge number of potential candidates, classification errors and subjectivity would make it difficult to replicate findings. Finally, a fully automated classification strategy also allows for the processing of large numbers of artificial sources that can be used to assess completeness. Although we do not do that here, we do intend to insert artificial sources throughout our analysis of the full data set so as to have position-dependent completeness estimates. That work will be described in a subsequent paper. Of course, inherent subjectivity in the classification of the training sample will propagate to any automated technique.

While machine learning methods have the distinct advantages of being able to classify images orders of magnitude faster than a human and provide consistent results, a potential major drawback is the reliability of their predictions. Nonetheless, in some applications they have been shown to approach

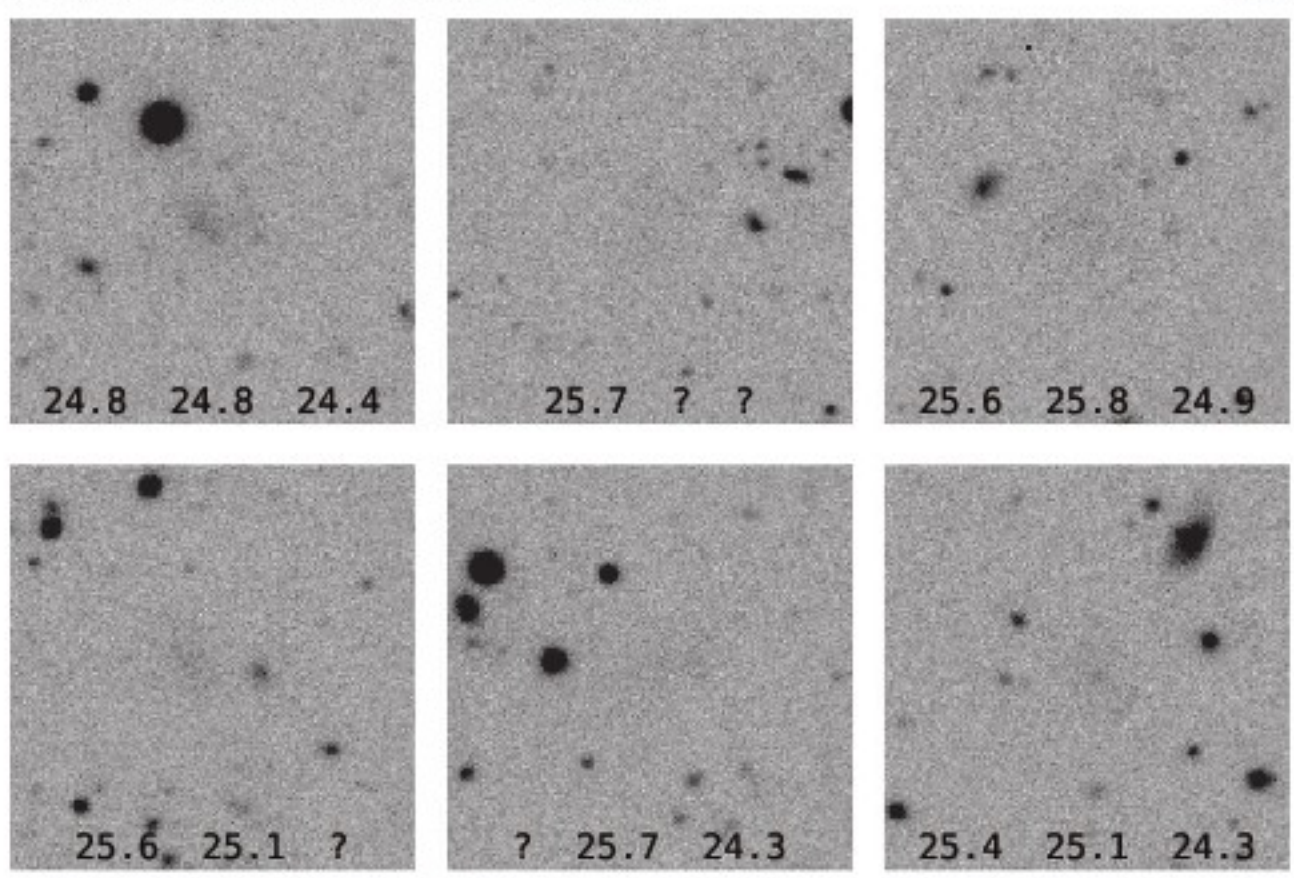


Figure 7. Examples of candidates with conflicting reviewer classifications. We present the strongest competing alternative classification to the UDG class with their names (if included in our catalog) and coordinates. Numbers at the bottom of each punel represent $\mu_{0,p}$, $\mu_{0,p}$, and $\mu_{0,p}$ respectively. A question mark indicates that no result is available for the associated band. All objects in the upper row were not ultimately classified as UDGs and are instead, from left to right, tidal debts (195.604, 26.8792), a background fluctuation (198.6044, 29.6972), and a faint galaxy cluster (192.9072, 27.345). All objects in the lower row were classified as UDGs, when we excluded that they might be, from left to right, tidal debris (SMDG 1228096+300844; 187.0398, 30.1457), a background fluctuation (SMDG 1311062+193524; 197.7758, 19.5901), or a galaxy cluster (SMDG 1307184+184326; 196.8266, 18.7240). As is evident, at the limit of the data the classification is difficult.

or even outperform human "experts" in classification accuracy (He et al. 2015). Modern algorithms initially developed for other purposes have recently been adapted for astronomical classifications (Fowler et al. 2017; Kim & Brunner 2017; Ackermann et al. 2018). We briefly present our approach below. A more detailed description of the methodology is presented in the Appendix, and an extended treatment will be presented by J. Kadowaki et al. (2018, in preparation). Here, our main goal is to test the self-consistency of our visual classifications. Can an automated technique demonstrate that our visual classifications are at least internally consistent?

We implement our automated classifier with a modified version of the DenseNet-201 deep learning model (Huang et al. 2016) supplied in the Keras machine learning library. This model was designed to classify color images and requires three channels of data for each image; therefore, we limit our data set to those candidates with observations in all three filters (1071 of 1079 candidates). This is the full sample of candidates after GALFIT screening but prior to any visual classification. We set aside 20% of the data set (215 candidates with 160 non-UDGs and 55 UDGs) to be used for testing only after all network parameters are finalized. The remaining 856 images are used to train the network. The accuracy after applying the trained model to the test set is 92.1%, with nine false positives and

We show all of the candidates from the test set with predictions by the classifier that differ from our visual classifications in Figure 8. Interestingly, we conclude that we mistakenly rejected the first candidate shown (panel (a)) and that it was correctly identified as a UDG candidate by the automated classifier. In our initial inspection we suspected that it could be a distant galaxy cluster, but on reinspection we agree with the automated classifier. Moreover, we visually classified another candidate (panel (b)) as a UDG candidate based on reviewing only the thumbnails. The classifier correctly rejected it, and a larger image drawn from the Legacy Survey Sky Viewer clearly shows it to be an isolated segment of a spiral arm associated with a large galaxy. We considered the faint object (c) to be an extension of a bright star just to the left of the thumbnail, although it appears to be separated from this region. Panels (d)-(f) are among those that had conflicting classifications between the two human reviewers. These either are generally very faint or could be composed of faint, high-z galaxies.

eight false negatives. These levels of accuracy are encouraging, but not necessarily optimized. In a subsequent study, we will explore alternative algorithms and compare results. For now, this degree of correspondence in our classification is adequate and suggests that our visual classification is internally selfconsistent.

¹¹ github.com/keras-team/keras

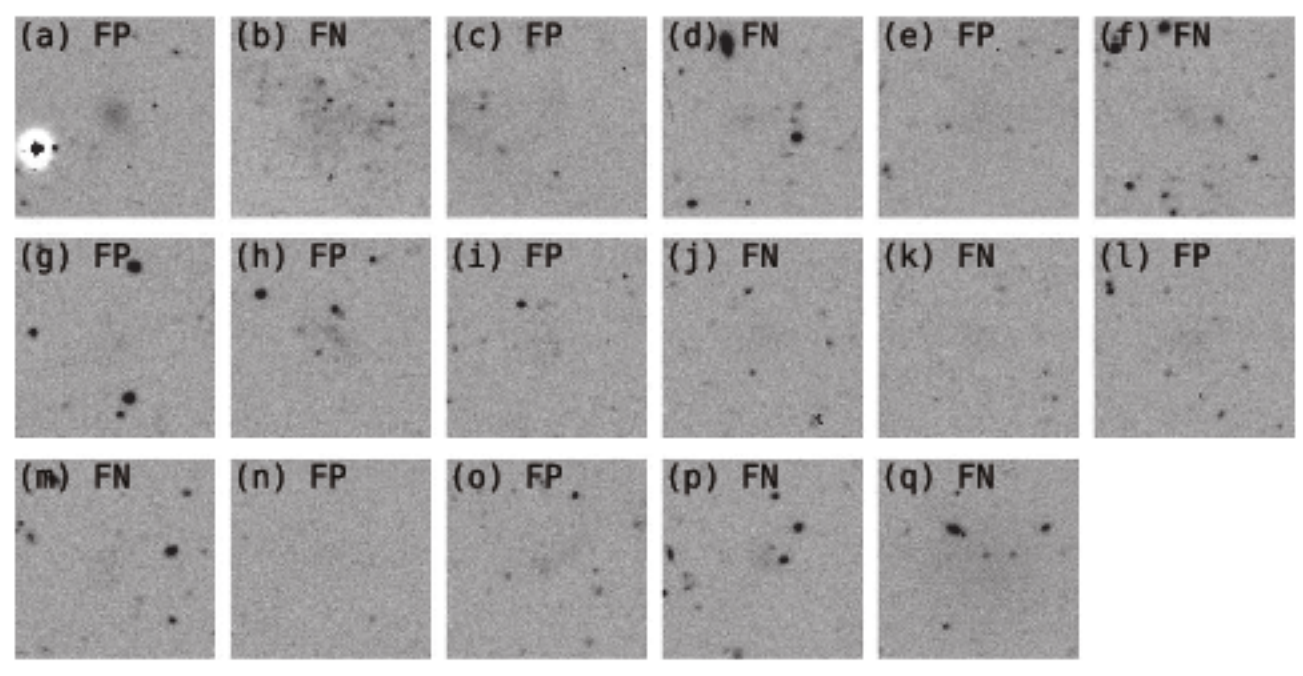


Figure 8. Classifications where predictions produced by an automated classifier differ from our visual classification. FN = false negative; FP = false positive relative to our visual classification. R.A., decl., and names (if included in our catalog) are provided for each panel. See the text for details. (a) 194.7899, 29.0068. (b) 189.0129, 28.0035. (c) 184.1296, 30.8345. (d) 185.0787, 32.5963; SMDG 1220189+323551. (e) 186.3063, 32.8416. (f) 187.04, 30.1449; SMDG 1228096+300844. (g) 186.0624, 25.9412. (h) 186.3714, 24.2447. (i) 187.47025, 27.5274. (j) 194.2139, 27.2277; SMDG 1256514+271338. (k) 195.5079, 28.0684; SMDG 1302019+280407. (l) 196.3744, 23.4967. (m) 183.3408, 29.5664; SMDG 1213219+293401. (a) 200.01857, 32.9523. (o) 202.7068, 27.3040. (p) 203.1018, 31.5587; SMDG 1332244+313331. (q) 184.1619, 26.9951; SMDG 1216389+265941.

3.6. The Catalog and Comparison with Previous Work

In Table 2 we present our final UDG catalog for this initial study of the region around the Coma Cluster. This selection of UDGs is based on our visual classification, with minor adjustments motivated by the automated classification. In print we present an example of the full table, showing only the first 10 entries, while the associated electronic table contains data for all 275 objects. We include coordinates both directly in the name of the object and in Columns (2) and (3). In the next three columns we present the g, r, and z central surface brightnesses. In the following three columns we present the structural parameters, effective radius (r_e) in arcsec, axis ratio (b/a), and major-axis position angle (θ) in degrees, where the latter is measured in the standard astronomical sense starting at north and measuring eastward on the sky. All of the aforementioned quantities are measured using a fixed n Sersíc model, with the structural measures being measured from the full stack of available images. In the next three columns we present the apparent magnitudes measured using floating n models. Uncertainties are those reported by GALFIT. We will revisit these uncertainties using simulated objects in subsequent work. None of the magnitudes are extinction corrected.

One of the principal motivating factors for starting our work in the region of the Coma Cluster is the existence of excellent prior surveys in the core of the cluster. These provide benchmarks against which we can test our false-negative and false-positive rates and our parameter estimation. We now describe our comparisons to two key samples.

3.6.1. van Dokkum et al. (2015a)

The catalog presented by van Dokkum et al. (2015a) based on the Dragonfly survey is dominated by the large UDGs that are also the focus of our survey. In Table 3 we present the cross-listed identifications for all of the UDGs presented by van Dokkum et al. (2015a) that have $r_a > 2.5$ kpc, for r_a as presented by those authors. Of the 30 UDGs from that study that satisfy this criterion, our catalog includes all but four. Two of those four (DF14 and 18) are excluded from our catalog because our fit to r_e is smaller than 2.5 kpc (one of which, DF14, just misses the cutoff with $r_e = 2.46$ kpc). During our visual definition of the training sample, DZ and RD disagreed on whether or not DF35 is tidal debris. Because disagreements are treated as non-UDGs, this object is excluded from our final list (Table 2). The final DF UDG that we excluded is DF12. This is a more difficult case to resolve because we rejected it on the basis of a low b/a, but on examination we find that the fitted model is poor and likely includes a nearby object. This is the one case of the four that is probably an incorrect exclusion on our part; however, because we cannot visually inspect all of the fits for the full SMUDGES survey, we exclude this object from our catalog and treat it as a false negative. We stress here that we did not miss any DF object of sufficient size (2.5 kpc) on the basis of a surface brightness limit on our part. We conclude that the Legacy Surveys data are suitable for UDG work at a competitive level with dedicated low surface brightness surveys (e.g., Dragonfly).

It is also valuable to determine whether we detect objects within the common survey footprint that van Dokkum et al. (2015a) did not. To be conservative in the sense that r_e measurement errors would not confuse the comparison, we consider only systems for which we measure $r_e > 3.5$ kpc. With this requirement, we find 15 objects in our catalog that lie within the DF footprint but that are not in their catalog (Figure 9). They noted confusion with the intracluster light as limiting their detections in the central regions of the cluster, but none of these 15 are within that region. They also emphasized isolated sources, so some of these may have been excluded as

13

Table 2 Ultra-diffuse Galaxy Properties

			Sérsic Index Fixed at $n = 1$					
α	δ	μ_{0g}	$\mu_{0,r}$	$\mu_{0,z}$	r _e (auc sec.)	b/a	θ	
183.033401	28.275014	24.4 ± 0.4	24.7 ± 0.5	24.8 ± 0.9	5.6 ± 0.6	0.88 ± 0.08	87 ± 28	21.1
183.035145	29.063514		24.2 ± 0.2	23.6 ± 0.5	6.1 ± 0.5	0.67 ± 0.05	156 ± 7	
183.189350	27.585352	24.7 ± 0.4	24.6 ± 0.4	23.6 ± 0.8	5.4 ± 0.6	0.59 ± 0.05	140 ± 7	21.4
183.275309	29.763710	24.0 ± 0.1	23.6 ± 0.1	23.0 ± 0.2	10.6 ± 0.2	0.79 ± 0.01	116 ± 3	18.3
183.341232	29.566810	25.4 ± 0.4	25.1 ± 0.4	111	6.4 ± 0.8	0.52 ± 0.05	76 ± 6	21.9
183.347943	26.777990	25.1 ± 0.3	24.6 ± 0.3	24.4 ± 0.6	6.4 ± 0.5	0.52 ± 0.03	80 ± 4	21.2
183.463343	28.352505	24.2 ± 0.2	24.0 ± 0.2	23.7 ± 0.4	5.5 ± 0.3	0.83 ± 0.04	41 ± 10	20.0
183.504356	29.534183	25.7 ± 0.4	25.5 ± 0.4		6.3 ± 0.9	0.72 ± 0.09	106 ± 16	21.8
183.616139	29.675991	25.2 ± 0.2	25.2 ± 0.4	24.3 ± 0.6	6.1 ± 0.5	0.70 ± 0.05	99 ± 8	21.6
183.674463	27.831858	24.6 ± 0.2	24.1 ± 0.1	23.8 ± 0.3	8.4 ± 0.4	0.97 ± 0.04	91 ± 43	19.4
	183.033401 183.035145 183.189350 183.275309 183.341232 183.347943 183.463343 183.504356 183.616139	183.033401 28.275014 183.035145 29.063514 183.189350 27.585352 183.275309 29.763710 183.341232 29.566810 183.347943 26.777990 183.463343 28.352505 183.504356 29.584183 183.616139 29.675991	$\begin{array}{cccccccccccccccccccccccccccccccccccc$	$\begin{array}{cccccccccccccccccccccccccccccccccccc$	$\begin{array}{c ccccccccccccccccccccccccccccccccccc$	$\begin{array}{c ccccccccccccccccccccccccccccccccccc$	$\begin{array}{c ccccccccccccccccccccccccccccccccccc$	$\begin{array}{c ccccccccccccccccccccccccccccccccccc$

(This table is available in its entirety in machine-readable form.)

Table 3
Cross-listing Large Daugenfly Coma UDGs with SMUDGES

Dangonfly ID	SMDG ID	Dragonfly ID	SMDG ID
DF01	SMDG 1259142+290717	DF28	SMDG 1259304+274450
DF03	SMDG 1302166+285717	DF29	SMDG 1258050+274358
DF04	SMDG 1302334+283452	DF30	SMDG 1253151+274115
DF06	SMDG 1256297+282640	DF31	SMDG 1255062+273727
DF07	SMDG 1257017+282325	DF32	SMDG 1256284+273706
DF08	SMDG 1301304+282228	DF34	SMDG 1256129+273250
DF09	SMDG 1256228+281955	DF35	111
DF12	111	DF36	SMDG 1255554+272736
DF14	111	DF39	SMDG 1258104+271911
DF15	SMDG 1258164+275330	DF40	SMDG 1258011+271126
DF17	SMDG 1301582+275011	DF41	SMDG 1257190+270556
DF18	11.1	DF42	SMDG 1301191+270315
DF19	SMDG 1304052+274804	DF44	SMDG 1300580+265835
DF25	SMDG 1259487+274639	DF46	SMDG 1300473+264700
DF26	SMDG 1300206+274712	DF47	SMDG 1255481+263352

nonisolated. As shown in the figure, these are mostly unambiguous detections, so the reason for their absence in the DF catalog is unclear without a closer examination of their images, but in some cases they may have exceeded the central surface brightness criterion in the DF evaluation. For 5 of the 15 we measure 24 mag arcsec⁻² < $\mu_{0,q}$ < 24.5 mag arcsec⁻²; the remainder are of lower central surface brightness.

3.6.2. Yagi et al. (2016)

This is the largest existing sample of UDGs in the Coma Cluster, although the gain in size comes mostly from identifying smaller and fainter systems than those found by van Dokkum et al. (2015a). For sources that do match our size criteria, we present the cross-listing in Table 4. There are two principal ways in which objects in the Yagi catalog can fail to be in ours. First, we do not detect the source or it fails the basic criteria, such as satisfying the parameter requirements from the initial Sérsic fit. Of the 75 objects in the published catalog that meet the size criteria, according to the effective radii presented by Yagi et al. (2016), 15 are absent from our catalog and are identified as such in the caption of Table 4. Of those, two (numbers 199 and 456 in the Yagi et al. 2016 catalog) are sufficiently bright (22.9 and 22.4 mag arcsec-2, respectively) that they were probably cleaned out of the images by our procedure. Four are sufficiently close to a bright object that they were either masked or removed as part of that object (231, 240, 257, and 370). Three were detected but failed the initial Sérsic fit screening (4, 218, 471). Finally, five are sufficiently faint or possible extensions of a nearby source that it is difficult to confirm them in our data (94, 310, 425, 453, 569). None of these sources have a corresponding SMDG number, and so they are not included in the table.

The second principal way in which objects in the Yagi catalog can fail to be in ours is if we rejected the candidate on the basis of our criteria. There are 26 such cases in Table 4, and we describe the reason for their exclusion from our catalog. For example, 21 of these, according to our measurements, either were too small or have a central surface brightness that is too bright. We conclude that despite the deeper imaging available for the Yagi et al. (2016) study, our survey for large UDGs is nearly as complete, with only a handful of examples of missed objects that could be attributed to our shallower image depth.

3.7. Remaining Problems and Limitations

None of the steps in our procedure are necessarily fully optimized, but certain aspects are perhaps easier to improve on than others. The procedure we describe consists of three basic phases. To recapitulate, first we remove as many sources from the images as possible to eliminate contamination for our smoothing or filtering of the data. Any large-scale residual features in our final cleaned images arise principally from issues that would require adjustment of the telescope and camera optics or observing procedures. Therefore, we conclude that this first phase is reasonably close to being optimized and do not anticipate significant gains from alternate approaches as applied to these same data. Second, we use wavelet filters to increase the S/N of low surface brightness features. There are a number of alternate approaches, and we suspect that there may be significant improvements possible in this step. Nevertheless, we are nearly complete in detecting known sources with the desired characteristics, so the incompleteness for these objects must be low. Improvements in this phase would perhaps allow us to reach even further into the low surface brightness population. Finally, the third phase is the classification of candidates. This step is important for sample purity and completeness. Our automated approach is an improvement over some coarse screening methods but will certainly improve once we have larger samples of confirmed, physically large UDGs. As we improve our search techniques, there will be natural refinements in this last step. We anticipate that for our final catalog the classification criteria and efficiency will change from that presented here. Completeness simulations will form an integral part of the final catalog.

A final complication on the completeness issue that must be acknowledged is that of clumpy, low surface brightness objects. Our artificial objects are smooth by construction, and we know so little about the internal structure of UDGs that we cannot yet create models of clumpy UDGs. We expect to detect UDGs that might have modest star-forming clumps, as long as they also have an underlying smooth stellar population, but estimating completeness for clump-dominated objects will be difficult.

Within the survey regions described here, we have not faced strong contamination from IR cirrus. Deeper surveys for low surface brightness detections have already been plagued by such emission (e.g., Duc et al. 2015), and we expect that some

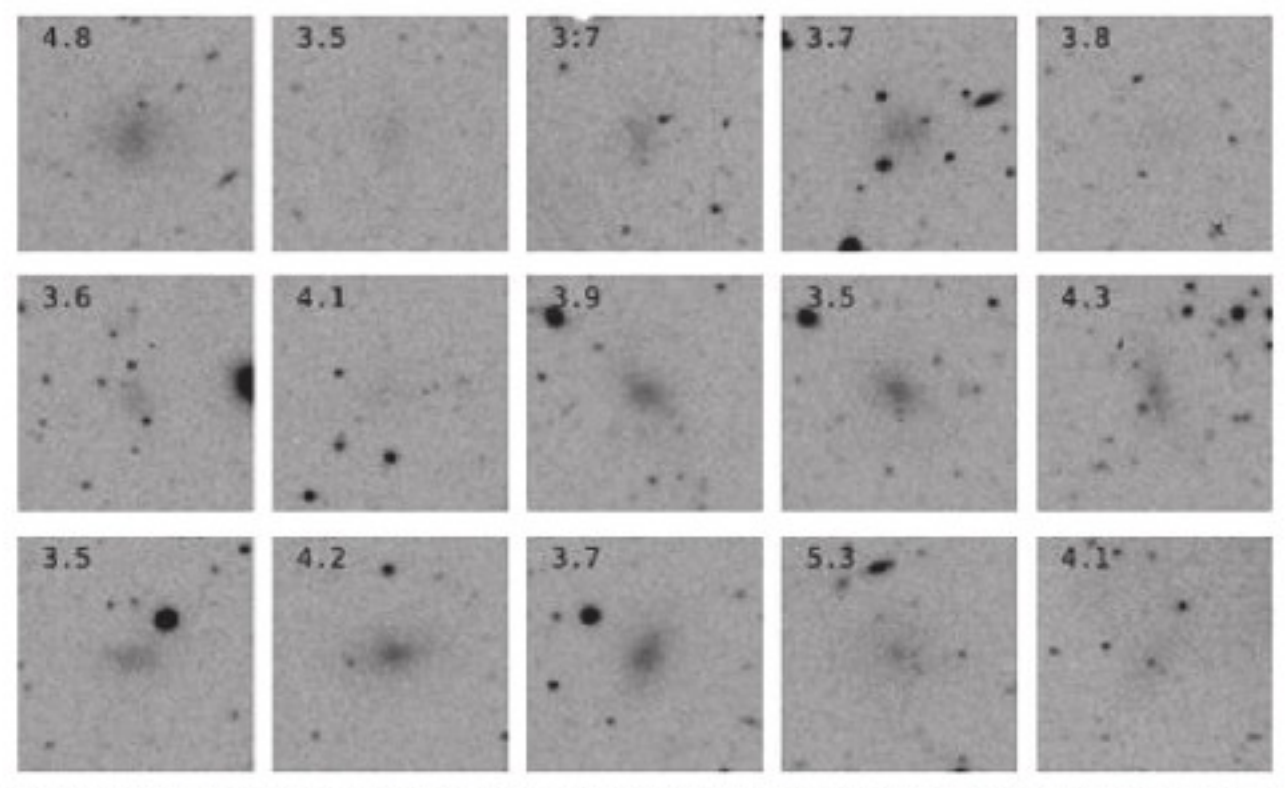


Figure 9. Our detections that lie within the DF footprint and have $r_e > 3.5$ kpc that are not included in the DF catalog. The measured r_e is given in the upper left corner of each panel. The UDGs (with coordinates) in order from top left to bottom right are SMDG 1253489+273934 (193.4536, 27.6594), SMDG 1254345+274046 (193.6439, 27.6796), SMDG 1255076+234407 (193.7816, 27.735), SMDG 1256265+285928 (194.1106, 28.9915), SMDG 1256514+271338 (194.2139, 27.278), SMDG 1257113+273405 (194.2966, 27.5881), SMDG 1257446+280907 (194.4357, 28.1515), SMDG 1258132+272522 (194.5548, 27.4229), SMDG 1259413+273148 (194.9222, 27.5299), SMDG 1300279+283730 (195.1164, 28.6251), SMDG 1301124+274525 (195.3014, 27.757), SMDG 1301158+271238 (195.316, 27.2107), SMDG 1303312+285716 (195.8799, 28.9546), SMDG 1303551+282120 (195.9795, 28.3555), and SMDG 1305016+290859 (196.2562, 29.1496). Boxes are 54° (\approx 26 kpc at the distance of Corna) on a side.

regions of the Legacy Surveys will also be too difficult for our work. We do not yet have an estimate for how large a fraction of the full survey may be affected.

4. Results

The UDG catalog we present contains 275 UDG candidates that have $r_e \gtrsim 5.73$, which corresponds to $\geqslant 2.5$ kpc at the distance of Coma and central surface brightness $\mu_{0,g} \geqslant$ 24 mag arcsec-2 (Table 2). The distribution of candidates in the absolute magnitude-size plane (assuming that they lie at the distance of the Coma Cluster) is presented in Figure 10. By construction, there is little overlap with the SDSS sample of galaxies, showing that this is almost exclusively a previously unknown population of galaxies over large areas of the sky, with the exception, of course, of previous UDG work in this area of sky (Section 3.6) and deeper surveys both in the Coma and other clusters (e.g., Graham & Guzmán 2003; van der Burg et al. 2016) and in the field (e.g., Greco et al. 2018). To place our UDGs in this figure, we assume that they lie at the distance of the Coma Cluster. Distance errors translate to motion of any individual galaxies parallel to the lines of constant surface brightness in the figure and therefore do not affect the previous conclusion. On average, $\mu_{0,g} \sim 25 \text{ mag arcsec}^{-2}$, with a tail of objects reaching to ~26 mag arcsec 2. Definitive conclusions regarding the size or magnitude distribution await a better understanding of the distances and the completeness across the parameter space.

4.1. Distance Constraints

Published spectroscopic redshifts, and therefore distance estimates, exist for fewer than 20 Coma UDGs and only a few outside of Coma (van Dokkum et al. 2015b, 2017; Kadowaki et al. 2017; Alabi et al. 2018). We continue to work to expand this sample using both optical spectroscopy (Kadowaki et al. 2018, in preparation) and radio observations of the 21 cm line to possibly detect the HI-rich UDGs within this same area of sky (A. Karunakaran et al. 2018, in preparation). However, this work will always be limited to a small fraction of all identified UDGs. We must address the challenge of understanding what the 2D distribution of UDG candidates on the sky (Figure 11) implies for the true 3D distribution and how best to estimate the distance to at least a subset of UDGs.

The relationship between the physical and apparent clustering properties of galaxies provides a constraint on the redshifts
of a population (Rahman et al. 2016). At its simplest, this
argument underpins the interpretation that the bulk of the
original Coma UDGs (van Dokkum et al. 2015a) lie at the
distance of the Coma Cluster because they so evidently
congregate around the galaxy cluster. This interpretation has
been confirmed with a small number of spectroscopic redshifts
(van Dokkum et al. 2015b; Kadowaki et al. 2017; Alabi et al.
2018). We find a similar overabundance of UDGs in our survey
(Figure 12), extending further from the Coma center to at least
the virial radius, roughly 3 Mpc (Kubo et al. 2007). In analogy
to the previous claims, it is plausible to conclude that the bulk
of these UDGs are also at the distance of Coma.

Table 4
Cusss-listing Large Yagi Coma UDGs with SMUDGES

Koda ID	Code	SMDG ID	Keda ID	Code	SMDG ID
11		SMDG 1300580+265835	443	В	SMDG 1258403+283905
13	111	SMDG 1301158+271238	486	111	SMDG 1259142+290717
14	111	SMDG 1301191+270315	494	111	SMDG 1256514+271338
16	B/S	SMDG 1301224+264950	501	111	SMDG 1257190+270556
22	S	SMDG 1302148+270843	507	111	SMDG 1258011+271126
37	C	SMDG 1300356+272951	526	В	SMDG 1256489+273650
53	111	SMDG 1301124+274525	553	111	SMDG 1257243+274343
92	В	SMDG 1300217+281341	571	111	SMDG 1257534+273202
93	111	SMDG 1300206+274712	577	111	SMDG 1258050+274358
98	S	SMDG 1300231+274820	581	111	SMDG 1258104+271911
165	111	SMDG 1301582+275011	583	111	SMDG 1258132+272522
166	В	SMDG 1301584+275454	584	111	SMDG 1258145+272429
168	S	SMDG 1302013+280508	629	S	SMDG 1257346+275440
178	111	SMDG 1300279+283730	641	111	SMDG 1257515+274923
194	111	SMDG 1301304+282228	649	S	SMDG 1258033+280805
212	S	SMDG 1302013+291222	653	S	SMDG 1258078+275444
215	111	SMDG 1302166+285717	654	S	SMDG 1258067+280112
230	В	SMDG 1259174+270140	660	111	SMDG 1258164+275330
215	***	SMDG 1302166+285717	654	S	SMDG 1258067+280112
230	В	SMDG 1259174+270140	660	111	SMDG 1258164+275330
281	***	SMDG 1259413+273148	680	***	SMDG 1257017+282325
285	***	SMDG 1259487+274639	695	C	SMDG 1257470+284643
320	***	SMDG 1258472+280724	698	C	SMDG 1257506+283756
328	В	SMDG 1258495+274216	739	***	SMDG 1255062+273727
348	111	SMDG 1259088+275736	743	S	SMDG 1255201+273027
352	111	SMDG 1259106+275415	774	111	SMDG 1256129+273250
390	S	SMDG 1259503+281123	782	***	SMDG 1256284+273706
407	S	SMDG 1300054+275333	787	111	SMDG 1256391+274055
416	A	SMDG 1300092+280829	819	В	SMDG 1255584+280357
436	S	SMDG 1300292+275924	851	111	SMDG 1256228+281955

Note. The large Yagi et al. (2016) UDG candidates that do not have counterparts in our detection catalog, prior to cuts made on size, brightness, and morphology, are 4, 94, 199, 218, 231, 240, 257, 275, 310, 370, 425, 453, 456, 471, and 569. The Code column presents our reason for excluding the candidate from our final UDG catalog (B = too bright; S = too small; A = too elongated; C = classified as other type of source).

Beyond the immediate vicinity of Coma, it is more difficult to associate UDGs with specific features seen in the normal galaxy distribution (Figure 11). There are locations where there is concurrence between the distribution of UDGs and SDSS galaxies and other locations where there is not. We label three of the interesting features as A, B, and C in the figure. Features A and C in the UDG distribution appear to match local largescale structure features near the Coma Cluster. These are analogous to the structures observed in the UDG distribution within the Abell 168 field (Román & Trujillo 2017a). They allow us to define subsamples beyond the Coma Cluster for which distance by association is possible. However, there are two concerns. First, feature B, which on the basis of the SDSS galaxy density one might have expected to be as evident as feature A, is not readily visible in the UDG distribution. Furthermore, feature C seems much richer in UDGs than a visual impression of the SDSS distribution might suggest. Such variations could point to interesting physical differences in the relative abundance of UDGs, or to errors introduced by associating UDGs too closely to their brighter cousins. In particular, for feature C, which is the result of the projection of sources along the right edge of the redshift wedge diagram (Figure 13), contributions come from a local overdensity, a broad overdensity at the distance of Coma, and an overdensity somewhat beyond Coma.

Such correspondences, either real or accidental, between the UDGs and normal galaxies can be evaluated more quantitatively. Presuming that the UDGs share similar physical correlation behavior to that of normal galaxies, the redshift slice for which the normal galaxy angular correlation function is a best match to the angular correlation function of the UDGs is likely to contain the bulk of the UDG sample. For example, comparing the angular correlation function of all of the normal galaxies that are projected outside of the center of Coma (where there is an obvious correlation between normal galaxies and UDGs), within 18 Mpc of the Coma Cluster (to limit ourselves to the area for which we have so far identified UDGs), and have $cz \leq 10,000 \,\mathrm{km \, s^{-1}}$ to that of the UDG sample yields a poor match (Figure 14, left panel). When we instead limit the comparison to normal galaxies within a narrow redshift strip that contains the Coma Cluster and associated structures $(6000 < cz/(km s^{-1}) < 8000)$, we find excellent agreement, especially at large angular separation where we will be sensitive to distance effects (Figure 14, right panel). We conclude that this sample of UDGs, which was chosen to be large in angular extent, is also predominantly one of physically large UDGs because it is mostly near the distance of Coma and the associated large-scale structure. This is a statement for the sample as a whole, but unfortunately it says little about the location of any particular UDG candidate. A full mathematical treatment of this approach will be presented elsewhere along the lines of that performed by Rahman et al. (2016), once we have a larger spectroscopic redshift sample to confirm the estimated redshift distributions.

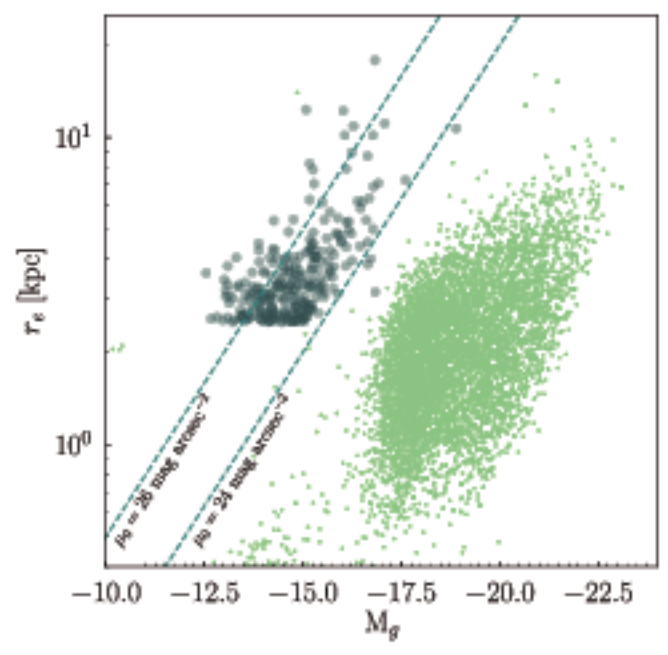


Figure 10. Absolute magnitude-size relation for the SDSS galaxies within the survey tegion and for $c\xi < 10,000 \,\mathrm{km \, s^{-1}}$ (smaller, lighter points) and the UDGs (larger, darker points). The absolute magnitudes of the UDGs are estimated by adopting a luminosity distance of 102.7 Mpc, consistent with Coma membership, for all. An incorrect distance assumption will slide a galaxy along the constant central surface brightness lines (dushed). The lines represent the loci of UDGs with b/a = 1 and central surface brightnesses of either 24 or 26 mag arcsec⁻² in the g band.

4.2. Size Distribution

Given a narrow range of surface brightness within r_e , the velocity dispersion of a galaxy, and hence the enclosed mass, is proportional to a power of r_e (Zaritsky 2017). Because our survey is limited to about a ± 1 mag range in surface brightness (Figure 10), we expect the physically largest systems to be the most massive and interesting. The largest confirmed UDGs, those with existing spectroscopic redshifts, are DF08 with $r_e = 4.4$ kpc and DF44 with $r_e = 4.6$ kpc (van Dokkum et al. 2015a, 2017; Kadowaki et al. 2017), and there are a few others that are slightly smaller but still have $r_e > 4$ kpc (Kadowaki et al. 2017). So far, this appears to be the upper end of the UDG size distribution.

The inferred size distribution of our UDGs (assuming that they lie at the distance of Coma) is qualitatively consistent with the size distribution of SDSS galaxies in the region (Figure 15) and shows a similar rapid decline toward larger sizes. The distance assumption is based on the earlier comparison of angular correlation functions, from which we concluded that the bulk of our UDG sample lies at roughly the distance of the Coma Cluster. This inference is supported by the redshift distribution of the SDSS galaxies in this region (Figure 13), where the dominant structure is a filament that includes the Coma Cluster and there are several large voids in the foreground to Coma. For both UDGs and SDSS galaxies, objects with $r_e > 5$ kpc are quite rare (particularly considering galaxies with $M_g > -20$).

There are a number of candidate UDGs with $r_e > 5$ kpc. We show in Figure 16 that even the UDGs with $4 < r_e/\text{kpc} < 6$ congregate around the Coma Cluster, demonstrating that the bulk of these are indeed at the distance of Coma, but that the UDGs with $r_e > 6$ kpc do not, suggesting that these are not physically associated with the Coma Cluster and therefore not at that distance. These are likely to be in the foreground and so have smaller physical sizes than we assigned them. In fact, some congregation of these "largest" UDGs is seen near what we have labeled feature C, which we previously noted is likely a superposition of both a local overdensity and overdensities at and beyond the Coma distance. Furthermore, some of these candidates have been spectroscopically confirmed as local in ongoing work (Kadowaki et al. 2018, in preparation). Nevertheless, there appear to be a significant number of analogs to DF08 and DF44 in size that have yet to be spectroscopically confirmed, both within the Coma Cluster and in the field.

Combining a quantitative version of this analysis and a much larger sample of UDG candidates and SDSS galaxies could lead to a determination of the upper end of the UDG size distribution. The angular correlation between UDG candidates and SDSS galaxies, where we can use the redshifts of the SDSS galaxies to isolate slices in the 3D distribution, will vanish when selecting UDGs that would be larger than those existing in reality.

4.3. Color Distribution

The star formation history of large UDGs is critical to establishing the physical reason for the apparent low star formation efficiency of these systems. DF44, for example, is estimated to have a total mass close to that of the Milky Way and yet only contain 1% as many stars (van Dokkum et al. 2015b). Has star formation ceased in all UDGs? Is it driven by environmental factors? Large samples such as that presented here, with colors, can begin to address such questions.

With the data in hand we examine broadband colors, g - z, across the whole sample and as a function of environment. To minimize the effect of noisy measurements, we choose to define our g - z measurement as the difference in corresponding central surface brightnesses. This could introduce a bias if UDGs have color gradients, but there is no measurement yet of systematic color gradients. In Figure 17 we compare the color-magnitude distribution to SDSS galaxies within 2° of Coma that are at the distance of Coma (0.018 < z < 0.028). We plot color against z-band magnitude, which is our best proxy for stellar mass. The UDGs span a range of colors from as red as the extrapolated sloped red sequence to well into the blue cloud. One interesting aspect of the figure is that there are only a few objects that are redder than the extrapolated red sequence. Given that one potential source of contamination is high-redshift galaxy clusters (see Gonzalez et al. 2001), it is reassuring that we are not detecting a large population of such red objects.

It is evident from this color-magnitude diagram (CMD) that even large UDGs must span a range of formation scenarios given the diverse properties. These large UDGs are not, entirely, fully quenched galaxies that follow directly from the SDSS red sequence population. Interpreting the CMD is not entirely straightforward because there are both mean age and metallicity effects. For two galaxies with the same stellar mass and mean age, the mean stellar metallicity can be quite different depending on the star formation history and the chemical enrichment history. Spectroscopic analysis of UDG populations, as recently done (Ferré-Mateu et al. 2018; Gu et al. 2018; Ruiz-Lara et al. 2018), is a more robust approach that can help constrain the range of options. Even so, CMDs are valuable

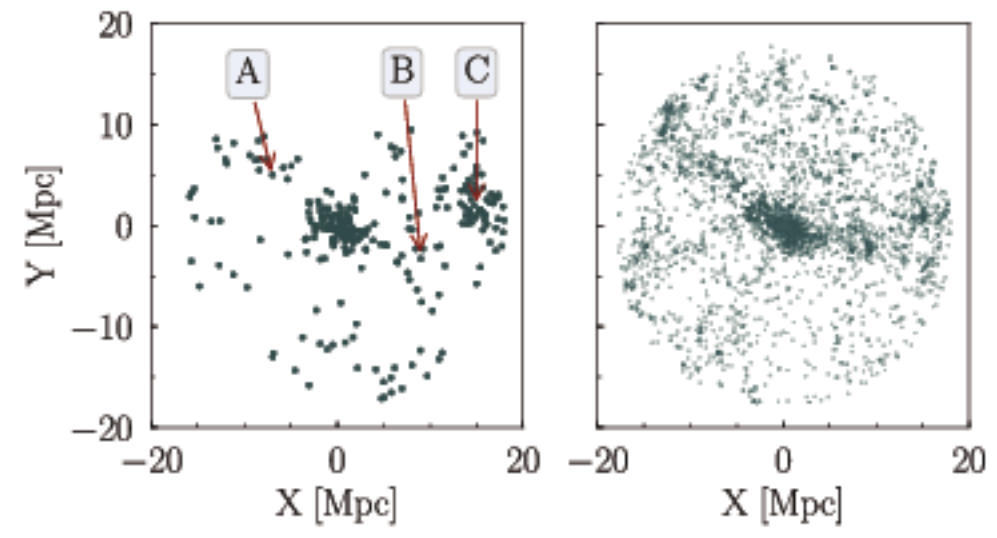


Figure 11. Projected distribution of UDGs (left panel) and SDSS galaxies (right panel) on the sky centered on the Coma Cluster. We plot in physical units assuming that all galaxies are at the Coma distance to provide guidance on the scale of the visible structures, which are at the distance of Coma. The UDGs represent our entire sample of 275. The SDSS galaxies include only those with recessional velocity $c_0^2 < 10,000 \, \mathrm{km \ s}^{-1}$ and within a projected separation of 18 Mpc from the center of the Coma Cluster. In addition to the clear clustering of both UDGs and SDSS galaxies in the Coma Cluster, there are three other features in common that are labeled and discussed in the text. North is up and east to the left. On the sky, this figure represents a region with a radius of $\sim 10^\circ$. Our UDG survey has no data at $Y \gtrsim 10 \, \mathrm{Mpc}$ (see Figure 1). The lettered labels refer to structures discussed in Section 4.1.

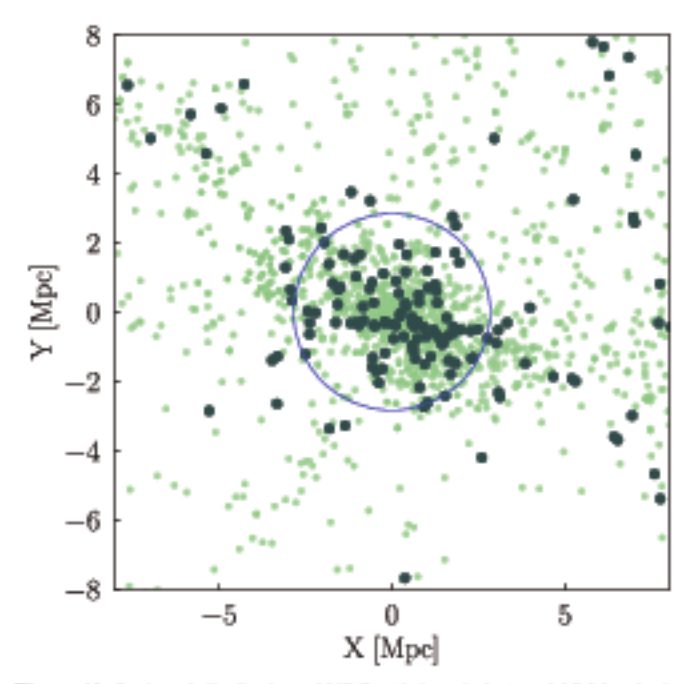


Figure 12. Projected distribution of UDGs (darker circles) and SDSS galaxies (lighter circles) on the sky centered on the Coma Cluster. We plot in physical units assuming that all UDGs are at the Coma distance. The SDSS galaxies include only those with recessional velocity 5500 km s⁻¹ < ez < 8500 km s⁻¹. The blue circle represents the virial radius, as reported by Kubo et al. (2007). North is up and east to the left.

because they can define samples or highlight the most interesting objects for follow-up spectroscopy.

To investigate how the colors may differ as a function of environment over the survey region, we divide the sample by color (Figure 18). We select the red sequence galaxies visually and extrapolate the slope to fainter magnitudes (shown in Figure 17). The blue galaxies are simply those that are at least 0.1 mag bluer than the blue side of the defined red sequence

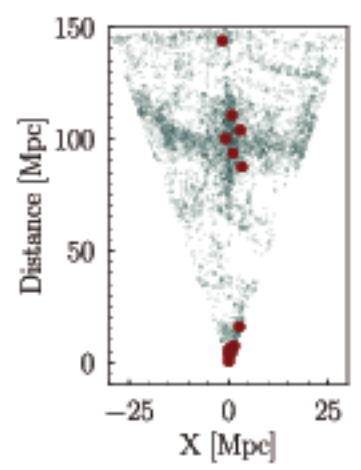


Figure 13. SDSS galaxy wedge diagram for the Coma region. The abscissa corresponds to projected distances from the Coma Cluster along R.A. The ordinate corresponds to Hubble flow velocity distances assuming $H_0 = 70 \text{ km s}^{-1} \text{ Mpc}^{-1}$. The observer is at the lower vertex, and the stretching of the Coma Cluster along the line of sight is the well-known "finger of God" effect. East is to the left. Large circles show the distances of individual UDGs determined from spectroscopic redshifts, obtained by Kadowaki et al. (2017), Kadowaki et al. (2018, in preparation), or the NASA Europalactic Database (NED).

region. There are two clear results in the figure. First, both red and blue UDGs are found in the vicinity of the Coma Cluster, although there is a preponderance of red galaxies. Once kinematics are available for a larger number of these, it will be interesting to determine whether there are indications of different dynamical histories for UDGs split by color. Second, feature C is proportionally more evident among the blue UDGs than the other overdensities. To some degree this can be an artifact of small numbers, but it may also reflect the higher level of contamination by nearby, smaller low surface brightness galaxies that we have discussed before. Distinguishing whether this is a physical result or due to contamination will be straightforward with statistics from a larger survey.

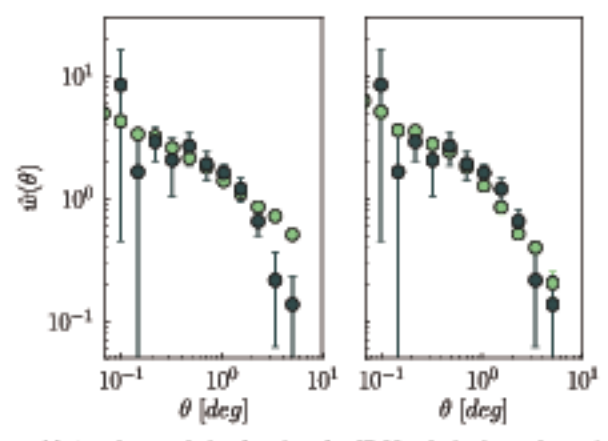


Figure 14. Angular correlation functions for SDSS galaxies beyond a projected radius of 3 Mpc from the Coma Cluster and within a projected radius of 18 Mpc with measured recessional velocities, c_Z , <10,000 km s⁻¹ (lighter filled circles with no error bars, left panel), the subset of these same galaxies that have c_Z corresponding to the Coma velocity (6000 km s⁻¹ < c_Z < 8000 km s⁻¹; lighter filled circles with no error bars, tight panel), and our sample of UDGs, selected over the same projected radius range (darker filled circles with error bars, both panels). The improved agreement at larger angular separations between the UDGs and Coma SDSS galaxies (right panel) suggests, under the assumption that the UDGshave a similar two-point correlation function in real space, that the majority of our UDGs are at the distance of the Coma Cluster.

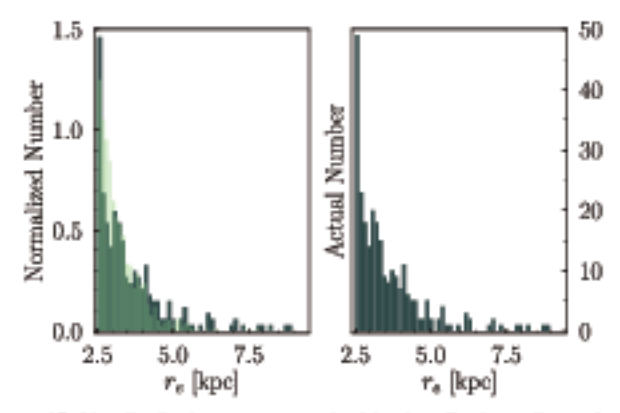


Figure 15. Size distribution as parameterized by the effective radius r_e for the SDSS galaxies in the survey volume (light-green histogram in the left panel) and the UDGs (dark-green histogram in both panels). For comparison, histograms are normalized to have unit area in the left panel. Galaxies with $r_e > 5$ kpc are rare in both samples. For the UDGs, we estimate r_e assuming that they all lie at the distance to Coma. Therefore, some of the unusually large systems may simply be much closer to us than the Coma Cluster. The UDG size distribution, if most lie at the distance of Coma and its associated large-scale structure, is consistent with that of SDSS galaxies.

5. Plans for the Full SMUDGES Program

The current analysis explores roughly 300 deg². The completed DESI imaging footprint is envisioned to extend to 14,000 deg². Even assuming that some sizable portion is not usable for our purposes owing to extreme IR cirrus contamination, we may be facing something in the neighborhood of 10,000 deg² of high-quality imaging, about 33 times more than that which we present here. Such sky coverage would suggest that we will identify a final sample of thousands of UDGs of large angular extent. This, in turn, helps highlight some daunting challenges in context.

The original processing run of the data presented here required about 30 days on a single desktop-quality machine and utilized more than 3 TB of storage, suggesting that the full analysis would require well over 3 yr of CPU time and more

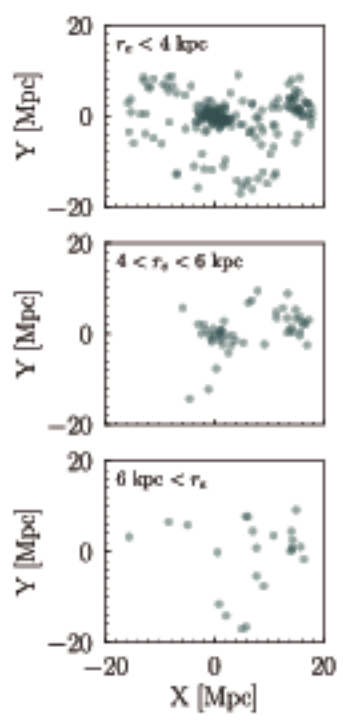


Figure 16. Spatial distribution of UDGs of different sizes. The abundance of large UDGs ($4 < r_e/\text{kpc} < 6$) in the Coma Cluster demonstrates that the large inferred physical sizes cannot be entirely due to enroneous adopted distances. The lack of any corresponding concentration suggests that inferred sizes >6 kpc are, at least, mostly incorrect. Orientation is the same as in Figure 11.

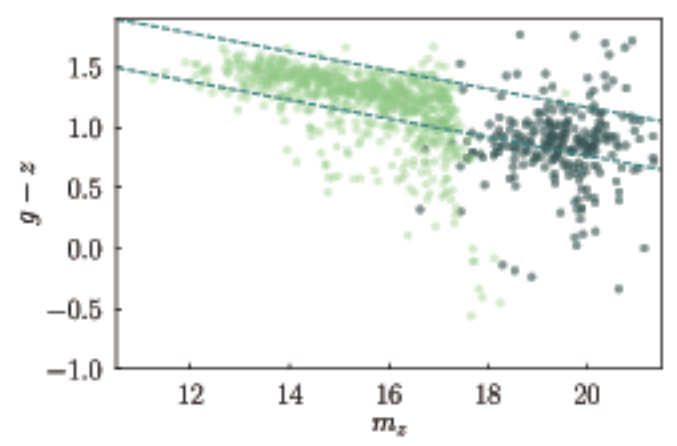


Figure 17. Color-apparent magnitude diagram for SDSS galaxies with 0.018 < z < 0.028 within 2° of the Coma Cluster (light green) and for our UDGs (dark green). Colors for the UDGs are measured as the difference in modeled central surface brightnesses. The UDGs span the range of colors of the SDSS galaxies. The dashed lines indicate the region defined by eye to follow the Coma Cluster and sequence. For galaxies at the distance of the Coma Cluster, the abscissa corresponds to $-24.6 < M_z < -13.6$.

than 100 TB of storage. This is a significant but not overwhelming challenge. However, one is also likely to require many runs with artificial sources to determine completeness corrections. That work will be the subject of a subsequent study in this series, and one may, for a variety of reasons, want to repeat at least parts of the original data processing. Now we have ported the pipeline to a high-performance computer (HPC) on which we can process data at a rate of ∼1 hr per exposure. There are typically ≈3 exposures deg⁻², so processing the nearly 10,000 deg² of the full survey will require ≈30,000 hr. We expect to use ∼30 cores on the HPC, so

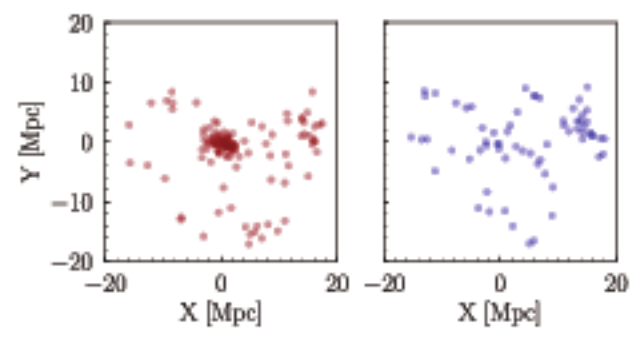


Figure 18. Spatial distribution of UDGs depending on g = z color. The red sequence (left panel) and blue cloud (right panel) selection is described in the text. There is slight evidence for clustering near the Coma Cluster for the blue galaxies, and most red galaxies are found in the Coma Cluster or the other structures identified in Figure 11.

approximately 6 weeks of computer time is required. The enterprise will take somewhat longer than this because there will undoubtedly be instances where human intervention is needed to address a problem. Nevertheless, this timescale is eminently practical. Regarding the disk space requirements, we will compress our data by ~6 and only save processed images. This approach suggests a requirement of ~15 TB.

The data processing and UDG identification are composed of several steps, some of which one might want to revisit and improve. As such, we will save intermediate steps. For example, it is possible that a new object identification procedure, either in the original source selection or in the subsequent "morphological" classification, will be developed, and one would simply want to run that on the cleaned images. These intermediate steps are not presented with this paper, but our intent is to make them easily available for the full survey.

The second, and much more serious, challenge is the lack of distance information for the UDG candidates. With an initial outlay of four nights of spectroscopic time on the Large Binocular Telescope (LBT), Kadowaki et al. (2017) obtained redshifts for five UDGs. At this rate we would require over 200 LBT nights just to observe the UDGs identified in this study, not the full sample we expect. We have also begun a program to target UDGs at 21 cm wavelengths because we expect, on the basis of the significant fraction with blue colors (Figure 17) and recent HI results (Spekkens & Karunakaran 2018), that at least some UDGs have significant gas reservoirs. Although we do not yet have results to report with regard to the sample presented here, similar observations (Spekkens & Karunakaran 2018) suggest that such observations can provide redshifts, although only moderately more efficient in terms of large telescope time. Even so, these observations have great potential to also provide a measurement of the internal kinematics and a direct measure of the gas content of UDGs, both of which will be critical in understanding the physical nature of UDGs. Nevertheless, we cannot expect to have spectroscopic redshifts for the bulk of our final UDG sample for the foreseeable future.

6. Summary

We present our first batch processing of DESI pre-imaging data of a region around the Coma Cluster in search of large $(r_e \gtrsim 5.0\%)$ 3 or equivalently $\geqslant 2.5$ kpc for those systems at the distance of the Coma Cluster) UDGs. We have termed this program as an effort that is Systematically Measuring Ultra-Diffuse Galaxies (SMUDGes). Due to the large data volume, a search through all of the DES1 pre-imaging data must be automated. We have developed a complete pipeline that (1) queries the data repository, (2) retrieves the data, (3) performs some additional basic data reduction to prepare that data, (4) subtracts all high surface brightness objects and corrects for extended emission from the brightest of those, (5) wavelet-transforms the residual image, (6) identifies significant peaks of emission in a series of those transformed images, (7) compares results from various photometric bands, (8) rejects defects and distinguishes among real sources of emission using machine learning methods, and (9) fits simple models to the stacked image of UDG candidates to do the final selection for large UDGs and provide their basic parameters. The pipeline is working on a high-performance cluster and is ready to continue processing the full survey.

We illustrate the results obtained with this pipeline by presenting a catalog of UDGs drawn from an area covering ≈290 deg² centered on the Coma Cluster. By centering on Coma, we are able to compare our detections directly to those from two recent surveys for UDGs (van Dokkum et al. 2015a; Yagi et al. 2016). Those surveys cover a significantly smaller area, but all cover the core of the Coma Cluster. From a comparison of results, we conclude that we are achieving comparable sensitivity and that where there are distinctions between our catalog and the literature, the differences arise from details of the object classification rather than the detections themselves.

We present a catalog of 275 candidate large UDGs. Using the catalog, we show that the majority of our UDGs are likely to be at roughly the distance of Coma based both on the number of galaxies that congregate around Coma and on the details of the angular correlation function. Accepting this result, we conclude that our sample contains a significant number of analogs of DF44 in size, where the effective radius exceeds 4 kpc. The conclusion is further confirmed by the angular clustering of these apparently large UDGs at the location of the Coma Cluster. In contrast, systems whose effective radius would exceed 6 kpc do not cluster near Coma, and we conclude that for these systems we are overestimating the distance and the size by incorrectly associating them with Coma.

We find that the g-z color of UDGs spans the full range from the red sequence to the blue edge of the blue cloud. As such, even the large UDGs are likely to reflect a range of formation histories. However, the majority have colors that are consistent with being low stellar mass versions of red sequence galaxies. Additional evidence for a range of processes being at play in UDG formation is that we find an overabundance of blue UDG candidates in the lower-density enhancements and the field. Redshifts are necessary to confirm that these are physically large galaxies.

The statistical treatment of large UDG samples will enable us to circumvent the critical challenge that we will be lacking spectroscopic redshifts for the majority of this sample. As such, we will benefit from the largest possible samples. Our analysis of the Legacy Surveys in search of UDGs, which we refer to as SMUDGes, promises to be the best such source until the advent of analogous analysis of the deeper LSST imaging.

D.Z., R.D., J.K., and H.Z. acknowledge financial support from NASA ADAP NNX12AE27G and NSF AST-1713841.
A.D.'s research is supported by the National Optical Astronomy Observatory. D.M.D. acknowledges support by Sonderforschungsbereich (SFB) 881 "The Milky Way System" of the German Research Foundation (DFG), particularly through sub-project A2. An allocation of computer time from the UA Research Computing High Performance Computing (HPC) at the University of Arizona and the prompt assistance of the associated computer support group are gratefully acknowledged.

This research has made use of the NASA/IPAC Extragalactic Database (NED), which is operated by the Jet Propulsion Laboratory, California Institute of Technology, under contract with NASA.

The Legacy Surveys consist of three individual and complementary projects: the Dark Energy Camera Legacy Survey (DECaLS; NOAO Proposal ID no. 2014B-0404; Pls: David Schlegel and Arjun Dey), the Beijing-Arizona Sky Survey (BASS; NOAO Proposal ID no. 2015A-0801; Pls: Zhou Xu and Xiaohui Fan), and the Mayall z-band Legacy Survey (MzLS; NO AO Proposal ID no. 2016A-0453; Pl: Arjun Dey). DECaLS, BASS, and MzLS together include data obtained, respectively, at the Blanco telescope, Cerro Tololo Inter-American Observatory, National Optical Astronomy Observatory (NOAO); the Bok telescope, Steward Observatory, University of Arizona; and the Mayall telescope, Kitt Peak National Observatory, NOAO. The Legacy Surveys project is honored to be permitted to conduct astronomical research on Iolkam Du'ag (Kitt Peak), a mountain with particular significance to the Tohono O'odham Nation.

NOAO is operated by the Association of Universities for Research in Astronomy (AURA) under a cooperative agreement with the National Science Foundation.

This project used data obtained with the Dark Energy Camera (DECam), which was constructed by the Dark Energy Survey (DES) collaboration. Funding for the DES Projects has been provided by the U.S. Department of Energy, the U.S. National Science Foundation, the Ministry of Science and Education of Spain, the Science and Technology Facilities Council of the United Kingdom, the Higher Education Funding Council for England, the National Center for Supercomputing Applications at the University of Illinois at Urbana-Champaign, the Kavli Institute of Cosmological Physics at the University of Chicago, the Center for Cosmology and Astro-Particle Physics at The Ohio State University, the Mitchell Institute for Fundamental Physics and Astronomy at Texas A&M University, Financiadora de Estudos e Projetos, Fundação Carlos Chagas Filho de Amparo, Financiadora de Estudos e Projetos, Fundação Carlos Chagas Filho de Amparo a Pesquisa do Estado do Rio de Janeiro, Conselho Nacional de Desenvolvimento Cientifico e Tecnologico and the Ministerio da Ciencia, Tecnologia e Inovacao, the Deutsche Forschungsgemeinschaft, and the Collaborating Institutions in the Dark Energy Survey. The Collaborating Institutions are Argonne National Laboratory, the University of California at Santa Cruz, the University of Cambridge, Centro de Investigaciones Energeticas, Medioambientales y Tecnologicas-Madrid, the University of Chicago, University College London, the DES-Brazil Consortium, the University of Edinburgh, the Eidgenossische Technische Hochschule (ETH) Zurich, Fermi National Accelerator Laboratory, the University of Illinois at Urbana-Champaign, the Institut de Ciencies de l'Espai (IEEC/CSIC), the Institut de Fisica d'Altes Energies, Lawrence Berkeley National Laboratory, the Ludwig-Maximilians Universitat

Munchen and the associated Excellence Cluster Universe, the University of Michigan, the National Optical Astronomy Observatory, the University of Nottingham, The Ohio State University, the University of Pennsylvania, the University of Portsmouth, SLAC National Accelerator Laboratory, Stanford University, the University of Sussex, and Texas A&M University.

BASS is a key project of the Telescope Access Program (TAP), which has been funded by the National Astronomical Observatories of China, the Chinese Academy of Sciences (the Strategic Priority Research Program "The Emergence of Cosmological Structures" grant no. XDB09000000), and the Special Fund for Astronomy from the Ministry of Finance. The BASS is also supported by the External Cooperation Program of Chinese Academy of Sciences (grant no. 114A11KYSB20160057) and the Chinese National Natural Science Foundation (grant no. 11433005).

The Legacy Survey team makes use of data products from the Near-Earth Object Wide-field Infrared Survey Explorer (NEOWISE), which is a project of the Jet Propulsion Laboratory/California Institute of Technology. NEOWISE is funded by the National Aeronautics and Space Administration.

The Legacy Surveys imaging of the DESI footprint is supported by the Director, Office of Science, Office of High Energy Physics of the U.S. Department of Energy under contract no. DE-AC02-05CH1123; by the National Energy Research Scientific Computing Center, a DOE Office of Science User Facility under the same contract; and by the U.S. National Science Foundation, Division of Astronomical Sciences under contract no. AST-0950945 to NOAO.

Facility: Blanco.

Software: galfit (Peng et al. 2002), keras (Chollet et al. 2015), lmfit (Newville et al. 2014), scipy (Jones et al. 2001), sep (Barbary 2016), sextractor (Bertin & Amouts 1996).

Appendix Deep Learning Classifier

We selected the DenseNet-201 model for our initial testing because their results suggest that it might provide better accuracy than other recent algorithms when trained on relatively small data sets (Huang et al. 2016). The Keras version of this application is designed to classify 1000 categories and requires modification to accommodate a binary decision (UDG or not UDG). Therefore, the softmax final layer is replaced with a dense layer with a sigmoid activation as a single output. This is preceded by a global average pooling layer to reduce overfitting (Lin et al. 2013). The Keras implementation of this model also eliminated the dropout layers (Srivastava et al. 2014) that were part of the original version (Huang et al. 2016). Because of our small data set, we added this function back into the transition layers to further reduce overfitting. All layers of the model are allowed to vary during training. The base layers are initially assigned weights derived from the Imagenet data set (Russakovsky et al. 2014), while weights of the modified top layers are randomly assigned.

Our 201 × 201 pixel thumbnails are resized to 150 × 150 and then divided into a train/validation set (80%) and a separate test set (20%). The test set is not evaluated until all hyperparameters are finalized. The train/validation set was further divided into four folds to be used for cross-validation. Two versions are created for each fold. One version contains the original data required for validation, and the other is

augmented and used for training. Augmentation is needed to expand our limited data set and consists of random flipping, rotation, and translation of the original images. To prevent excessive padding of image edges, rotation is limited to 10° and translation is limited to a distance of 7 pixels from the center after random flipping. The original data set is unbalanced with an excess of non-UDGs, and therefore, UDGs are augmented with six transformations, while others are augmented with three. Cross-validation is performed for each fold, with the training set composed of the augmented versions of the other three folds and testing done with the unaugmented version. For optimization, we use Adam (Kingma & Ba 2014) with $beta_1 = 0.9$, $beta_2 = 0.999$, epsilon = 0.0000001, and decay = 0.0. The data set is trained for 100 epochs with an initial learning rate of 0.00005. The learning rate is decreased by multiplying by 0.3 every 25 epochs. The Keras implementation of binary cross-entropy is used as the loss function. We investigated dropout fractions of 0.2, 0.3, and 0.4 and found that a value of 0.3 gave the best results during cross-validation. After finalizing hyperparameters using cross-validation, the four augmented folds are combined into a single training set and run on the test set to provide our final results as described in Section 3.5.

ORCID iDs

Dennis Zaritsky © https://orcid.org/0000-0002-5177-727X
Arjun Dey ® https://orcid.org/0000-0002-4928-4003
Jennifer Kadowaki ® https://orcid.org/0000-0002-3767-9681
Huanian Zhang
(张华年) ® https://orcid.org/0000-0002-0123-9246
Ananthan Karunakaran ® https://orcid.org/0000-00018855-3635
David Martínez-Delgado ® https://orcid.org/0000-00033835-2231
Mubdi Rahman ® https://orcid.org/0000-0003-1842-6096
Kristine Spekkens ® https://orcid.org/0000-0002-0956-7949

```
References
Abraham, R. G., & van Dokkum, P. G. 2014, PASP, 126, 55
Ackennunn, S., Schawinksi, K., Zhang, C., Weigel, A. K., & Turp, M. D.
   2018, MNRAS, 479, 415
Agertz, O., & Kmytsov, A. V. 2016, ApJ, 824, 79
Alabi, A., Fearé-Mateu, A., Romanowsky, A. J., et al. 2018, MNRAS,
Amorisco, N. C., & Loeb, A. 2016, ApJ L, 459, L51
Amorisco, N.-C., Monuchesi, A., Agnello, A., & White, S. D. M. 2018,
  MNRAS, 475, 4235
Anisimova, E., Páta, P., & Blažek, M. 2011, AcPol, 51, 9
Barbary, K. 2016, JOSS, 1, 58
Beasley, M. A., Romanowsky, A. J., Pota, V., et al. 2016, ApJL, 819, 20
Bennet, P., Sand, D. J., Crmojević, S. K., Zantsky, D., & Karunakanan, A.
   2017, ApJ, 850, 109
Bestin, E., & Arnouts, S. 1996, A&AS, 117, 393
Blukeslee, J. P., Tonry, J. L., & Metzger, M. R. 1997, AJ, 114, 482
Carleton, T., Errani, R., Cooper, M., Kaplinghat, M., & Peñarsubia, J. 2018,
Chan, T. K., Kereš, D., Wetzel, A., et al. 2018, MNRAS, 478, 906
Chollet, F., et al. 2015, Keras, GitHub, https://github.com/keras-team/keras-
Conselice, C. J., Gullagher, J. S., III, & Wyse, R. F. G. 2003, AJ, 125, 66
Dulcunton, J. J., Spergel, D. N., Gunn, J. E., Smith, M., & Schneider, D. P.
   1997, AJ, 114, 635
Dumiani, F., Maggio, A., Micela, G., & Sciortino, S. 1997, ApJ, 483, 350
DePoy, D. L., Abbott, T., Annis, J., et al. 2008, Proc. SPIE, 7014, 70140E
DESI Collaboration, et al. 2016a, arXiv:1611.0036
DEST Collaboration, et al. 2016b, arXiv:1611.0037
```

```
Dey, A., Schlegel, D. J., Lang, D., et al. 2018, AJ, submitted (arXiv:1804.
   08657)
Di Cintio, A., Brook, C. B., Dutton, A. A., et al. 2017, MNRAS, 466, L1
Disney, M. J. 1976, Natur, 264, 573
Duc, P.-A., Cuillandre, J.-C., Kambal, E., et al. 2015, MNRAS, 446, 120
Feiré-Mateu, A., Alabi, A., Forbes, D. A., et al. 2018, MNRAS, 479, 4891
Flaugher, B., Diehl, H. T., Honscheid, K., et al. 2015, AJ, 150, 150
Forbes, D. A., Alabi, A., Romanowsky, A. J., et al. 2016, MNRAS, 458, L44
Fowler, L., Schawinski, K., Brandt, B.-E., & Widmer, N. 2017, AAS Meeting,
  229, 236, 10
Georgiev, I. Y., Puzia, T. H., Goudfrooij, P., & Hilker, M. 2010, MNRAS,
  406, 1967
Gonzulez, A. H., Zuritsky, D., Dulcanton, J. J., & Nelson, A. 2001, ApJS,
Gmhun, A. W., & Guzmán, R. 2003, AJ, 125, 2936
Greco, J., Greene, J. E., Stmuss, M. A., et al. 2018, ApJ, 857, 104
Gu, M., Conroy, C., Law, D., et al. 2018, ApJ, 859, 37
Harris, W. E., Blakeslee, J. P., & Harris, G. L. H. 2017, ApJ, 836, 67
Harris, W. E., Harris, G. L. H., & Alessi, M. 2013, ApJ, 772, 82
Häussler, B., McIntosh, D. H., Burden, M., et al. 2007, ApJS, 172, 615
He, K., Zhang, X., Ren, S., & Sun, J. 2015, arXiv:1502.01852
Huang, G., Liu, Z., van der Mauten, L., & Weinberger, K. Q. 2016,
  arXiv:1608.06993
Impey, C., & Bothun, G. 1989, ApJ, 341, 89
Impey, C., Bothun, G., & Malin, D. 1988, ApJ, 330, 634
Jones, E., Oliphant, T., Peterson, P., et al. 2001, SciPy: Open Source Scientific
   Tools for Python, https://www.scipy.org
Kadowaki, J., Zaritsky, D., & Donnerstein, R. L. 2017, ApJL, 838, 21
Kim, E. J., & Brunner, R. J. 2017, MNRAS, 464, 4463
Kingma, D. P., & Ba, J. 2014, arXiv:1412.6980
Kniazev, A. Y., Grebel, E. K., Pustilnik, S. A., et al. 2004, AJ, 127, 704
Koda, J., Yugi, M., Yamanoi, H., & Komiyama, Y. 2015, ApJL, 807, 2
Kubo, J. M., Stebbins, A., Annis, J., et al. 2007, ApJ, 671, 1466
Lee, M. G., Kang, J., Lee, J. H., & Jung, I. S. 2017, ApJ, 844, 157
Leisman, L., Haynes, M. P., Janowiecki, S., et al. 2017, ApJ, 842, 133L.
Lim, S., Peng, E. W., Cote, P., et al. 2018, ApJL, 862, 82
Lin, M., Chen, Q., & Yun, S. 2013, arXiv:1312.4400
Makarov, D. I., Sharina, M. E., Kanachentseva, V. E., & Karachentsev, I. D.
   2015, A&A, 581, 82
Murtínez-Delgado, D., Läsker, R., Sharina, M., et al. 2016, AJ, 151, 96
Merritt, A., van Dokkum, P., Danieli, S., et al. 2016, ApJ, 833, 168
Mihos, J. C., Dunell, P. R., Feirarese, L., et al. 2015, ApJL, 809, 21
Muñoz, R. P., Eigenthaler, P., Puzia, T. H., et al. 2015, ApJL, 813, 15
Newville, M., Stensitzki, T., Allen, D. B., & Ingargiola, A. 2014, LMFIT: Non-
  Linear Least-Square Minimization and Curve-Fitting for Python, zenodo,
   doi:10.5281/zenodo.11813
Oke, J. B. 1964, ApJ, 140, 689
Oke, J. B., & Gunn, J. E. 1983, ApJ, 266, 713
Peng, C. Y., Ho, L. C., Impey, C. D., & Rix, H.-W. 2002, AJ, 124, 266
Penny, S. J., Conselice, C. J., De Rijcke, S., & Held, E. V. 2009, MNRAS,
  393, 1054
Prole, D. J., Duvies, J. I., Keemin, O. C., & Duvies, L. J. M. 2018, MNRAS,
   478, 667
Rahman, M., Mendez, A. J., Ménard, B., et al. 2016, MNRAS, 460, 163
Roberts, M. S. 1976, ComAp., 6, 105
Román, J., & Tsujillo, I. 2017a, MNRAS, 468, 703
Román, J., & Tsujillo, I. 2017b, MNRAS, 468, 4039
Rubin, V. C., Thonnutd, N., & Ford, W. K., Jr. 1978, ApJL, 225, 107
Ruiz-Lam, T., Beasley, M. A., Falcón-Barroso, J., et al. 2018, MNRAS,
   478, 2034
Russukovsky, O., Deng, J., Su, H., et al. 2014, arXiv:1409.0575
Sundage, A., & Binggeli, B. 1984, AJ, 89, 919
Schlegel, D., Abdalla, F., Abraham, T., et al. 2011, arXiv:1106.1706
Schombert, J. M., & Bothun, G. D. 1988, AJ, 95, 1389
Schwartzenberg, J. M., Phillipps, S., Smith, R. M., Couch, W. J., &
   Boyle, B. J. 1995, MNRAS, 275, 121
Shi, D. D., Zheng, X. Z., Zhuo, H. B., et al. 2017, ApJ, 846, 26
Sifón, C., van der Burg, R. F. J., Hoekstra, H., Muzzin, A., & Herbonnet, R.
   2018, MNR AS, 473, 3747
Spekkens, K., & Karunakama, A. 2018, ApJ, 855, 28
Sprayberry, D., Impey, C. D., Irwin, M. J., & Bothun, G. D. 1997, ApJ,
Srivustavu, N., Hinton, G., Krizhevsky, A., Sutskever, I., & Salakhutdinov, R.
   2014, J. Much. Leam. Res, 15, 1929
```

Starck, J.-L., & Murtagh, F. 2006, Astronomical Image and Data Analysis

(Berlin: Springer)

Valdes, F., Gruendl, R. & DES Project 2014, adass XXIII, 485, 379 van der Burg, R. F., Muzzin, A., & Hoekstm, H. 2016, A&A, 590, 20 van der Burg, R. F. J., Hoekstra, H., Muzzin, A., et al. 2017, A&A, 607, 79 van Dokkum, P., Abraham, R., Brodie, J., et al. 2016, ApJL, 828, L6 van Dokkum, P., Abraham, R., Romanowsky, A. J., et al. 2017, AplL, 844, L11 van Dokkum, P. G., Abusham, R., Merritt, A., et al. 2015a, Apl L, 798, 45 van Dokkum, P. G., Romanowsky, A. J. m., Abraham, R., et al. 2015b, ApJL., 804, L26

Venhola, A., Peletier, R., Laurikainen, E., et al. 2017, A&A, 608, 142 Wittmann, C., Lisker, T., Ambuchew Tilahun, L., et al. 2017, MNRAS, 470, 1512 Wolf, J., Martinez, G. D., Bullock, J. S., et al. 2010, MNRAS, 406, 1220

Yagi, M., Koda, J., Komiyama, Y., & Yamanoi, H. 2016, ApJS, 225, 11 Yozin, C., & Bekki, K. 2015, MNRAS, 452, 937

Zaritsky, D. 2017, MNRAS, 464, 110L

Zaritsky, D., Crnojević, D., & Sand, D. J. 2016, ApJL, 826, L9